Chapter 15 in Modeling for Casting and Solidification Processingx, O. Yu, editor, Marcel Dekker, New York, NY, 2001, pp. 499-540.

Continuous Casting of Steel

Brian G. Thomas

Department of Mechanical and Industrial Engineering
University of Illinois at Urbana-Champaign
1206 West Green Street
Urbana, IL 61801, U.S.A.

I. Introduction

Continuous casting is used to solidify most of the 750 million tons of steel produced in the world every year. Like most commercial processes, continuous casting involves many complex interacting phenomena. Most previous advances have been based on empirical knowledge gained from experimentation with the process. To further optimize the design and improve the continuous casting process, mathematical models are becoming increasingly powerful tools to gain additional quantitative insight. The best models for this purpose are mechanistic models based on the fundamental laws and phenomena which govern the process, because they are more reliably extended beyond the range of data used to calibrate them.

This chapter first presents an overview of the many interacting phenomena that occur during the continuous casting of steel. It then reviews some of the advanced mechanistic models of these phenomena and provides a few examples of the information and insights gained from them. These model applications focus on the mold region, where many continuous casting defects are generated.

II. Process Description

In the continuous casting process, pictured in Figure 1, molten steel flows from a ladle, through a tundish into the mold. It should be protected from exposure to air by a slag cover over each vessel and by ceramic nozzles between vessels. Once in the mold, the molten steel freezes against the water-cooled copper mold walls to form a solid shell. Drive rolls lower in the machine continuously withdraw the shell from the mold at a rate or "casting speed" that matches the flow of incoming metal, so the process ideally runs in steady state. Below mold exit, the solidifying steel shell acts as a container to support the remaining liquid. Rolls support the steel to minimize bulging due to the ferrostatic pressure. Water and air mist sprays cool the surface of the strand between rolls to maintain its surface temperature until the molten core is solid. After the center is completely solid (at the "metallurgical length") the strand can be torch cut into slabs.

III. Basic Phenomena

Some of the important phenomena which govern the continuous casting process and determine the quality of the product are illustrated in Figure 2. Steel flows into the mold through ports in the submerged entry nozzle, which is usually bifurcated. The high velocities produce Reynolds numbers exceeding 100,000 and fully-turbulent behavior.

Argon gas is injected into the nozzle to prevent clogging. The resulting bubbles provide buoyancy that greatly affects the flow pattern, both in the nozzle and in the mold. They also collect inclusions and may become entrapped in the solidifying shell, leading to serious surface defects in the final product.

The jet leaving the nozzle flows across the mold and impinges against the shell solidifying at the narrow face. The jet carries superheat, which can erode the shell where it impinges on locally thin regions. In the extreme, this may cause a costly breakout, where molten steel bursts through the shell.

Typically, the jet impinging on the narrow face splits to flow upwards towards the top free surface and downwards toward the interior of the strand. Flow recirculation zones are created above and below each jet. This flow pattern changes radically with increasing argon injection rate or with the application of electromagnetic forces, which can either brake or stir the liquid. The flow pattern can fluctuate with time, leading to defects, so transient behavior is important.

Liquid flow along the top free surface of the mold is very important to steel quality. The horizontal velocity along the interface induces flow and controls heat transfer in the liquid and solid flux layers, which float on the top free surface. Inadequate liquid flux coverage leads to nonuniform initial solidification and a variety of surface defects.

If the horizontal surface velocity is too large, the shear flow and possible accompanying vortices may entrain liquid flux into the steel. This phenomenon depends greatly on the composition-dependent surface tension of the interface and possible presence of gas bubbles, which collect at the interface and may even create a foam [1]. The flux globules then circulate with the steel flow and may later be entrapped into the solidifying shell lower in the caster to form internal solid inclusions.

The vertical momentum of the steel jet lifts up the interface where it impinges the top free surface. This typically raises the narrow face meniscus, and creates a variation in interface level, or “standing wave”, across the mold width. The liquid flux layer tends to become thinner at the high points, with detrimental consequences.

Transient fluctuations in the flow cause time-variations in the interface level which lead to surface defects such as entrapped mold powder. These level fluctuations may be caused by random turbulent motion, or changes in operating conditions, such as the sudden release of a nozzle clog or large gas bubbles.

The molten steel contains solid inclusions, such as alumina. These particles have various shapes and sizes and move through the flow field while colliding to form larger clusters and may attach to bubbles. They either circulate up into the mold flux at the top surface, or are entrapped in the solidifying shell to form embrittling internal defects in the final product.

Mold powder is added to the top surface to provide thermal and chemical insulation for the molten steel. This oxide-based powder sinters and melts into the top liquid layer that floats on the top free interface of the steel. The melting rate of the powder and the ability of the molten flux to flow and to absorb detrimental alumina inclusions from the steel depends on its composition, governed by time-dependent thermodynamics. Some liquid flux resolidifies against the cold mold wall, creating a solid flux rim which inhibits heat transfer at the meniscus. Other flux is consumed into the gap between the shall and mold by the downward motion of the steel shell, where it encourages uniform heat transfer and helps to prevent sticking.

Periodic oscillation of the mold is needed to prevent sticking of the solidifying shell to the mold walls, and to encourage uniform infiltration of the mold flux into the gap. This oscillation affects the level fluctuations and associated defects. It also creates periodic depressions in the shell surface, called “oscillation marks”, which affect heat transfer and act as initiation sites for cracks.

Initial solidification occurs at the meniscus and is responsible for the surface quality of the final product. It depends on the time-dependent shape of the meniscus, liquid flux infiltration into the gap, local superheat contained in the flowing steel, conduction of heat through the mold, liquid mold flux and resolidified flux rim, and latent heat evolution. Heat flow is complicated by thermal stresses which bend the shell to create contact resistance, and nucleation undercooling, which accompanies the rapid solidification and controls the initial microstructure.

Further solidification is governed mainly by conduction and radiation across the interfacial gap between the solidifying steel shell and the mold. This gap consists mainly of mold flux layers, which move down the mold at different speeds. It is greatly affected by contact resistances, which depend on the flux properties and shrinkage and bending of the steel shell, which may create an air gap. The gap size is controlled by the amount of taper of the mold walls, which is altered by thermal distortion. In addition to controlling shell growth, these phenomena are important to crack formation in the mold due to thermal stress and mold friction, which increases below the point where the flux becomes totally solid.

As solidification progresses, microsegregation of alloying elements occurs between the dendrites as they grow outward to form columnar grains. The rejected solute lowers the local solidification temperature, leaving a thin layer of liquid steel along the grain boundaries, which may later form embrittling precipitates. When liquid feeding cannot compensate for the shrinkage due to solidification, thermal contraction, phase transformations, and mechanical forces, then tensile stresses are generated. When the tensile stresses concentrated on the liquid films are high enough to nucleate an interface from the dissolved gases, then a crack will form.

After the shell exits the mold and moves between successive rolls in the spray zones, it is subject to large surface temperature fluctuations, which cause phase transformations and other microstructural changes that affect its strength and ductility. It also experiences thermal strain and mechanical forces due to ferrostatic pressure, withdrawal, friction against rolls, bending and unbending. These lead to complex internal stress profiles which cause creep and deformation of

the shell. This may lead to further depressions on the strand surface, crack formation and propagation.

Lower in the caster, fluid flow is driven by thermal and solutal buoyancy effects, caused by density differences between the different compositions created by the microsegregation. This flow leads to macrosegregation and associated defects, such as centerline porosity, cracks, and undesired property variations. Macrosegregation is complicated by the nucleation of relatively pure crystals, which move in the melt and form equiaxed grains that collect near the centerline.

Large composition differences through the thickness and along the length of the final product can also arise due to intermixing after a change in steel grade. This is governed by transient mass transport in the tundish and liquid portion of the strand.

IV. Model Formulation

Mathematical models are being applied to quantify and investigate interactions between these phenomena as a function of the controllable process parameters. Mechanistic models are based on satisfying the laws of conservation of heat, mass, force and momentum in an appropriate domain with appropriate boundary conditions. Each phenomenon considered is represented by term(s) in these governing equations. The equations are discretized using finite difference or finite element methods and are solved numerically with computers, which are becoming increasingly fast and affordable. Because of the overwhelming complexity, no model can include all of the phenomena at once. An essential aspect of successful model development is the selection of the key phenomena and the making of reasonable assumptions.

V. Flow through the Submerged Entry Nozzle

The geometry and position of the Submerged Entry Nozzle (SEN) are easy and inexpensive to change. These design variables have a critical influence on steel quality through their effect on the flow pattern in the mold. Fluid velocities in the nozzle have been calculated by solving the three-dimensional Navier Stokes equations for mass and momentum balance [2]. Turbulence is modeled by solving two additional partial differential equations for the turbulent kinetic energy, K (m^2/s^2) and the rate of turbulence dissipation, ε (m^2/s^3) and focusing on the time-averaged flow pattern.

Flow through the SEN is gravity driven by the pressure difference between the liquid levels of the tundish and the mold top free surfaces. This is generally not modeled, as the inlet velocity to the SEN is simply imposed based on the casting speed of interest. In practice, the flow rate is further controlled by other means which strive to maintain a constant liquid level in the mold. In one method, a "stopper rod" extends down through the tundish to partially plug the exit. In another method, a "slide gate" blocks off a portion of the SEN pipe section by moving a disk-shaped plate through a horizontal slit across the entire SEN. These flow-control devices strongly influence the flow pattern in the nozzle and beyond, so should be modeled.

Figure 3 shows a typical time-averaged flow pattern calculated in a 50% open slide gate system [3] using the finite difference program, FLUENT [4]. Multiphase flow effects, caused by the injection of argon gas in the upper tundish well just above the slide gate, were modeled by solving additional transport equations for the gas phase. Velocity vectors on the left and corresponding gas bubble fraction on the right show that gas collects in at least 5 different recirculation zones. The largest regions form in the cavity created by the slide gate, and just below the slide gate. Gas also collects in the corners above the slide gate and in the upper portion of oversized nozzle exit ports. In each of these zones, steel flow is minimal so gas bubbles tend to collect, leading to large bubble fractions in these regions. These bubbles might collide to form large pockets of gas. If large gas pockets are entrained into the downward flowing steel, they may cause detrimental sudden changes in flow pattern, such as "annular flow" [5]. The slide gate also creates significant asymmetry. In single phase flow with a 75% closed slide gate, twice as much fluid exits the port opposite the gate opening and with a shallower jet angle [6]. The random nature of gas bubbles diminishes this asymmetry (assuming annular flow does not occur).

Figure 4 shows a close-up of steady flow near a nozzle port [7]. One quarter of the nozzle is modeled using the finite element program, FIDAP, [8] by assuming two-fold symmetry. Flow exits only the bottom portion of the nozzle port, due to the oversized area of the port (90 x 60 mm) relative to the nozzle bore (76 mm diameter). This creates stagnant recirculating flow in the upper portion of the ports, where gas collects and alumina particles can attach to form clogs. Figure 3 also shows that the jet's momentum causes it to exit at a steeper downward angle than machined into the bottom edge of the ceramic nozzle port. This particular jet exits at a downward angle of 10˚, even though its nozzle has ports angled 15˚ upward.

The view looking into the nozzle (4b) reveals swirling flow with two recirculation zones spiraling outward from each port. Due to flow instabilities, one of these zones usually grows to dominate the entire port, leading to swirl in a particular direction. The swirl is stronger for larger, upward angled nozzles, and with a 90˚ aligned slide gate (which moves perpendicular to the direction pictured in Figure 3). After a jet with a single swirl direction enters the mold cavity, it deflects towards one of the wide faces, leading to asymmetric flow.

This model has been validated with experimental measurements [2] and applied to investigate the effects of nozzle design parameters, such as the shape, height, width, thickness and angles of the ports, on the jet leaving the nozzle [6]. This jet is characterized by its average speed, direction, spread angle, swirl, turbulence intensity, dissipation rate, ε, and degree of symmetry. These conditions can be used as input to a model of flow in the mold.

VI. Fluid Flow in the Mold

Due to its essentially turbulent nature, many important aspects of flow in continuous casting are transient and difficult to control. However, the time-averaged flow pattern in the mold is greatly influenced by the nozzle geometry, submergence depth, mold dimensions, argon injection rate, and electromagnetic forces.

A. Effect of Argon Gas Injection

One of the important factors controlling flow in the mold is the amount of argon injected into the nozzle to control clogging [9]. Because the injected gas heats quickly to steel temperature and expands, the volume fraction of gas bubbles becomes significant. Those bubbles which are swept down the nozzle into the mold cavity create a strong upward force on the steel jet flowing from the nozzle, owing to their buoyancy. A few models have been applied to simulate this complex flow behavior [9, 10].

Figure 5 shows two flow patterns in the upper region of a 220 x 1320 mm mold for 1 m/min casting speed, calculated using a 3-D finite-difference turbulent-flow model [8]. Bubble dispersion is modeled by solving a transport equation for the continuum gas bubble concentration, [9] assuming that turbulent diffusivity of the gas bubble mixture is the same as that of the fluid eddies [9]. Bubble momentum and drag are ignored, so each grid point is assumed to have only a single “mixture” velocity.

Without gas injection (Figure 5 a) the jet typically hits the narrow face and is directed upward and back along the top surface towards the SEN. Maximum velocities near the center of the top surface reach almost 0.2 m/s. With optimal argon, Figure 5 b), top surface velocities are greatly reduced. With too much argon, the jet may bend upward to impinge first on the top surface, and then flow along this interface towards the narrow face. Recirculation in the upper mold is then reversed and there are no longer separate recirculation zones above and below the jet. These changes in flow pattern may have important consequences for steel quality, discussed later in this Chapter.

B. Effect of Electromagnetic Forces

Electromagnetic forces can be applied to alter the flow in continuous casting in several different ways. A rotating magnetic field can be induced by passing electrical current through coils positioned around the mold. This forces electromagnetic "stirring" of the liquid in the horizontal plane of the strand. Alternatively, a strong DC magnetic field can be imposed through the mold thickness, which induces eddy currents in the metal. The resulting interaction creates a "braking" force which slows down the fluid in the flow direction perpendicular to the imposed field. Slower flow has several potential benefits: slower, more uniform fluid velocities along the top surface, more uniform temperature, [11] less inclusion entrapment in the solidifying shell below the mold, [12] and the ability to separate two different liquids to cast clad steel, where the surface has a different composition than the interior [13].

Electromagnetic phenomena are modeled by solving Maxwell's equations and then applying the calculated electromagnetic force field as a body force per unit volume in the steel flow equations [14]. Significant coupling between the electromagnetic field and the flow field may occur for DC braking, which then requires iteration between the magnetic field and flow calculations. Idogawa and coworkers applied a decoupled model to suggest that the optimal braking strategy was to impose a field across the entire width of the mold in two regions: above and below the nozzle inlet [14]. Care must be taken not to slow down the flow too much, or the result is the same as angling the ports to direct the jet too steeply downward: defects associated with freezing the meniscus. In addition, the field also increases some velocity components, which has been modeled to increase free surface motion in some circumstances [15].

Others have examined the application of electromagnetic fields near the meniscus to change the surface microstructure [16]. Finally, electromagnetic stirring both in and below the mold is reported to reduce centerline macrosegregation [17], presumably due to the flow effects on heat transfer and nucleation.

C. Transient Flow Behavior

Transient surges in the steel jets leaving the nozzle parts may cause asymmetric flow, leading to sloshing or waves in the molten pool [18]. Jet oscillations are periodic and increase in violence with casting speed, making them a particular concern for thin slab casting [19]. Huang has shown that a sudden change in inlet velocity creates a large transient flow structure, that appears to be a large vortex shed into the lower region of the liquid cavity [20]. Recent transient models have reproduced periodic oscillations of the jet, even with constant inlet conditions [21]. The consequences of nonoptimal flow, such as top surface level fluctuations are discussed next.

VII. Consequences of Fluid Flow in the Mold

The steady flow pattern in the mold is not of interest directly. However, it influences many important phenomena, which have far-reaching consequences on strand quality. These effects include controlling the dissipation of superheat (and temperature at the meniscus), the flow and entrainment of the top surface powder layers, top-surface contour and level fluctuations, the motion and entrapment of subsurface inclusions and gas bubbles. Each of these phenomena associated with flow in the mold can lead to costly defects in the continuous-cast product [22]. Design compromises are needed to simultaneously satisfy the contradictory requirements for avoiding each of these defects.

A. Superheat Dissipation

An important task of the flow pattern is to deliver molten steel to the meniscus region that has enough superheat during the critical first stages of solidification. Superheat is the sensible heat contained in the liquid represented by the difference between the steel temperature entering the mold and the liquidus temperature.

The dissipation of superheat has been modeled by extending the 3-D finite-difference flow model to include heat transfer in the liquid [23]. The effective thermal conductivity of the liquid is proportional to the effective viscosity, which depends on the turbulence parameters. The solidification front, which forms the boundary to the liquid domain, has been treated in different ways. Some researchers model flow and solidification as a coupled problem on a fixed grid. However, this approach is subject to convergence difficulties and requires a fine grid to resolve the thin porous mushy zone. In addition, properties such as permeability of this mush are uncertain and care must be taken to avoid any improper advection of the latent heat. An alternative approach for columnar solidification of a thin shell, such as found in the continuous casting of steel, is to treat the boundary as a rough wall fixed at the liquidus temperature [24]. This approach has been shown to match plant measurements in the mold region, where the shell is too thin to affect the flow significantly [23, 25, 26].

Figure 6 compares the measured temperature distribution in the mold [27] with recent calculations using a 3-D finite-difference flow model [28]. Incorporating the effects of argon on the flow pattern were very important in achieving the reasonable agreement observed. This figure shows that the temperature drops almost to the liquidus by mold exit, indicating that most of the superheat is dissipated in the mold. The hottest region along the top surface is found midway between the SEN and narrow face. This location is directly related to the flow pattern. The coldest regions are found at the meniscus at the top corners near the narrow face and near the SEN.

The cold region near the meniscus is a concern because it could lead to freezing of the meniscus, and encourage solidification of a thick slag rim. This could lead to quality problems such as deep oscillation marks, which later initiate transverse cracks. It can also disrupt the infiltration of liquid mold flux into the gap, which can induce longitudinal cracks and other surface defects. The cold region near the SEN is also a concern because, in the extreme, the steel surface can solidify to form a solid bridge between the SEN and the shell against the mold wall, which often causes a breakout. To avoid meniscus freezing problems, flow must reach the surface quickly. This is why flow from the nozzle should not be directed too deep.

The jet of molten steel exiting the nozzle delivers most of its superheat to the inside of the shell solidifying against the narrow face [23]. The large temperature gradients found part-way down the domain indicate that the maximum heat flux delivery to the inside of the solidifying shell is at this location near mold exit. If there is good contact between the shell and the mold, then this heat flux is inconsequential. If a gap forms between the shell and the mold, however, then the

reduction in heat extraction can make this superheat flux sufficient to slow shell growth and even melt it back. In the extreme, this can cause a breakout. Breakouts are most common at mold exit just off the corners, where contact is the poorest. This problem is worse with higher flow rates and non-uniform flow from the nozzle [23].

B. Top-Surface Shape and Level Fluctuations

The condition of the meniscus during solidification has a tremendous impact on the final quality of the steel product. Meniscus behavior is greatly affected by the shape of the top "free" surface of the liquid steel, and in particular, the fluctuations in its level with time. This surface actually represents the interface between the steel and the lowest powder layer, which is molten.

If the surface waves remain stable, then the interface shape can be estimated from the pressure distribution along the interface calculated from a simulation with a fixed boundary [29].

$$\text{standing wave height} = \frac{(\text{surface pressure - 1 atm})}{(\text{steel density - flux density})g} \qquad (1)$$

When casting with low argon and without electromagnetics in a wide mold, the interface is usually raised about 25 mm near the narrow face meniscus, relative to the lower interface found near the SEN. This rise is caused by the vertical momentum of the jet traveling up the narrow face and depends greatly on the flow pattern and flow rate. The rise in level increases as the density difference between the fluids decreases, so water / oil models of the steel / flux system tend to exaggerate this phenomenon. Recent models are being developed to predict the free surface shape coupled with the fluid flow [29]. Additional equations must be solved to satisfy the force balance, at the interface, involving the pressure in the two phases, shear forces from the moving fluids, and the surface tension. Numerical procedures such as the Volume of Fluid Method are used to track the arbitrary interface position.

The transient simulation of level fluctuations above a turbulent flowing liquid is difficult to model. However, a correlation has been found between the steady kinetic energy (turbulence) profile across the top surface and level fluctuations [20]. Figure 7 compares calculated turbulence levels [20] along the top surface of the moving steel with measured level fluctuations [30]. The flow calculations were performed using a steady-state, 3-D, turbulent K-ε finite-difference model of fluid flow in the mold. The observed agreement is expected because the kinetic energy contained in the moving fluid corresponds to the time-averaged velocity

fluctuations, which may be converted temporarily to potential energy in the form of a rise or fall in level.

For typical conditions, Figure 7 a), the most severe level fluctuations are found near the narrow face, where turbulence and interface level are highest. These level fluctuations can be reduced by directing the jet deeper and changing the flow pattern. It is interesting to note that increasing argon injection moves the location of maximum level fluctuations (and accompanying turbulence) towards the SEN at the central region of the mold, (0.5m away from the narrow faces in Figure 7 b). Casting at a lower speed with a smaller mold width means that steel throughput is less. This increases the volume fraction of argon, if the argon injection rate (liters / second) is kept constant. It is likely that the higher argon fraction increases bubble concentration near the SEN, where it lifts the jet, increases the interface level near the SEN, and produces the highest level fluctuations.

Sudden fluctuations in the level of the free surface are very detrimental because they disrupt initial solidification and can entrap mold flux in the solidifying steel, leading to surface defects in the final product. Level fluctuations can deflect the meniscus and upset the infiltration of the mold flux into the gap, building up a thick flux rim and leaving air gaps between the shell and the mold. Together, this can lead to deep, nonuniform oscillation marks, surface depressions, laps, bleeds and other defects. The thermal stress created in the tip of the solidifying shell from a severe level fluctuation has been predicted to cause distortion of the shell, which further contributes to surface depressions [31].

C. Top Surface Powder / Flux Layer Behavior

The flow of the steel in the upper mold greatly influences the top surface powder layers. Mold powder is added periodically to the top surface of the steel. It sinters and melts to form a protective liquid flux layer, which helps to trap impurities and inclusions. This liquid is drawn into the gap between the shell and mold, where it acts as a lubricant and helps to make heat transfer more uniform. The behavior of the powder layers is very important to steel quality and powder composition is easy to change. It is difficult to measure or to accurately simulate with a physical model, so is worthy of mathematical modeling.

A 3-D finite-element model of heat transfer and fluid flow has been developed of the top surface of the continuous caster to predict the thickness and behavior of the powder and flux layers [32].

The bottom of the model domain is the steel / flux interface. Its shape is imposed based on measurements in an operating caster, and the shear stress along the interface is determined through coupled calculations using the 3-D finite-difference model of flow in the steel. Uniform consumption of flux was imposed into the gap at the bottom edges of the domain along the wide and narrow faces. The model features temperature-dependent properties of the flux, with enhanced viscosity in the temperature range where sintering occurs and especially in the resolidified liquid flux, which forms the rim. Temperature throughout the flux was calculated, including the interface between the powder and liquid flux layers.

When molten steel flows rapidly along the steel / flux interface, it induces motion in the flux layer. If the interface velocity becomes too high, then the liquid flux can be sheared away from the interface, become entrained in the steel jet, and be sent deep into the liquid pool to become trapped in the solidifying shell as a harmful inclusion [1]. If the interface velocity increases further, then the interface standing wave becomes unstable, and huge fluctuations contribute to further problems.

The model results in Figure 8 show the calculated flux layer thickness relative to the assumed steel profile [32]. Input flow conditions were similar to those in Figure 5 a); maximum total powder and liquid flux thickness was 35 mm, and flux consumption was 0.6 kg/m^2. The flux layer was found to greatly reduce the steel velocity at the interface, due to its generally high viscosity relative to the steel. However, the rapid flow of steel along the interface was calculated to drag the liquid flux, in this case towards the SEN. This induces recirculation in the liquid flux layer, which carries powder slowly toward the narrowface walls, opposite to the direction of steel flow. The internal recirculation also increases convection heat transfer and melts a deeper liquid flux layer near the SEN. The result is a steel flux interface that is almost flat.

The thickness of the beneficial liquid flux layer is observed to be highly non-uniform. It is generally thin near the narrow face because the steel flow drags most of the liquid towards the center. The thinnest liquid flux layer is found about 150 mm from the narrow face. In this region, a flow separation exists where liquid flux is pulled away in both directions: toward the narrow face gap, where it is consumed, and towards the SEN. This shortage of flux, compounded by the higher, fluctuating steel surface contour in this region, makes defects more likely near the narrow face for this flow pattern. This is because it is easier for a level fluctuation to allow molten steel to touch and entrain solid powder particles. In addition, it is more difficult for liquid flux to feed continuously into the gap. Poor flux feeding leads to air gaps, reduced, non-uniform heat flow, thinning of the shell, and longitudinal surface cracks [30]. It is important

to note that changing the flow pattern can change the flow in the flux layers, with corresponding changes in defect incidence.

D. Motion and Entrapment of Inclusions and Gas Bubbles

The jets of molten steel exiting the nozzle carry inclusions and argon bubbles into the mold cavity. If these particles circulate deep into the liquid pool and become trapped in the solidifying shell, they lead to internal defects. Inclusions lead to cracks, slivers, and blisters in the final rolled product [22]. Trapped argon bubbles elongate during rolling and in low-strength steel, may expand during subsequent annealing processes to create surface blisters and "pencil pipes" [1].

Particle trajectories can be calculated using the Langrangian particle tracking method, which solves a transport equation for each inclusion as it travels through a previously-calculated molten steel velocity field. The force balance on each particle can include buoyancy and drag force relative to the steel. The effects of turbulence can be included using a "random walk" approach [4]. A random velocity fluctuation is generated at each step, whose magnitude varies with the local turbulent kinetic energy level. To obtain significant statistics, the trajectories of several hundred individual particles should be calculated, using different starting points. Inclusion size and shape distributions evolve with time, which affects their drag and flotation velocities. Models are being developed to predict this, including the effects of collisions between inclusions [33] and the attachment of inclusions to bubbles [3].

Particle trajectories were calculated in the above manner for continuous casting at 1 m/min through a 10-m radius curved-mold caster [3] using FLUENT [4]. Most of the argon bubbles circulate in the upper mold area and float out to the slag layer. This is because the flotation velocities are very large for 0.3 - 1.0 mm bubbles. Many inclusions behave similarly, as shown by three of the inclusions in Figure 9. Bubbles circulating in the upper recirculation region without random turbulent motion were predicted to always eventually float out. Bubbles with turbulent motion often touch against the solidification front. This occurs on both the inside and outside radius with almost equal frequency, particularly near the narrow faces high in the mold, where the shell is thin (<20mm). It is likely that only some of these bubbles stick, when there is a solidification hook, or other feature on the solidification front to catch them. This entrapment location does not correspond to pencil pipe defects.

A few bubbles manage to penetrate into the lower recirculation zone. Here, a very small argon bubble likely behaves in a similar manner to a large inclusion cluster. Specifically, a 0.15mm bubble has a similar terminal velocity to a 208-micron solid alumina inclusion, whose trajectories are plotted in Figure 16. These particles tend to move in large spirals within the slow lower recirculation zones, while they float towards the inner radius of the slab. At the same time, the bubbles are collecting inclusions, and the inclusions are colliding. When they eventually touch the solidifying shell in this depth range, entrapment is more likely on the inside radius. This could occur anywhere along their spiral path, which extends from roughly 1-3m below the meniscus. This distance corresponds exactly with the observed location of pencil pipe defects [3]. There is a slight trend that smaller bubbles are more likely to enter the lower zone to be entrapped. However, the event is relatively rare for any bubble size, so the lack of sufficient statistics and random turbulent motion mask this effect.

Recent work with a transient K-ε flow model [20] suggests that sudden changes to the inlet velocity may produce transient structures in the flow that contribute to particle entrapment. After an inlet velocity change, the large zone of recirculating fluid below the jet was modeled to migrate downwards like a shedding vortex. The particles carried in this vortex are then transported very deep into the liquid pool. Thus, they are more likely to become entrapped in the solidifying shell before they float out.

To minimize the problem of particle entrapment on the inside radius, some companies have changed their machine design from the usual curved mold design to a costly straight mold design. Through better understanding of the fluid dynamics using models, it is hoped that alternative, less expensive modifications to the nozzle geometry and casting conditions might be found to solve problems such as this one.

VIII. Composition Variation During Grade Changes

The intermixing of dissimilar grades during the continuous casting of steel is a problem of growing concern, as the demand for longer casting sequences increases at the same time as the range of products widens. Steel producers need to optimize casting conditions and grade sequences to minimize the amount of steel downgraded or scrapped. In addition, the unintentional sale of intermixed product must be avoided. To do this requires knowledge of the location and extent of the intermixed region and how it is affected by grade specifications and casting conditions.

A 1-D, transient mathematical model, MIX1D, has been developed to simulate the final composition distributions produced within continuous-cast slabs and blooms during an arbitrary grade transition [34]. The model is fully transient and consists of three submodels, that account for mixing in the tundish, mixing in the liquid core of the strand, and solidification. The three submodels have been incorporated into a user-friendly FORTRAN program that runs on a personal computer in a few seconds.

Figure 10 shows example composition distributions calculated using the model. All compositions range between the old grade concentration of 0 and the new grade concentration of 1. This dimensionless concept is useful because alloying elements intermix essentially equally [35]. This is because the turbulent mass diffusion coefficient, which does not depend on the element, is about 5 orders of magnitude larger than the laminar diffusion coefficient.

To ensure that the MIX1D model can accurately predict composition distribution during intermixing, extensive verification and calibration has been undertaken for each submodel [36]. The tundish submodel must be calibrated to match chemical analysis of steel samples taken from the mold in the nozzle port exit streams, or with tracer studies using full-scale water models. Figure 10 a) shows an example result for a small (10 tonne) tundish operation. The strand submodel was first calibrated to match results from a full 3-D finite-difference flow model, where an additional 3-D transport equation was solved for transient species diffusion [35]. Figure 10 b) shows reasonable agreement between the 3-D model and the simplified 1-D diffusion model. Figure 10 b) also compares the MIX1D model predictions with composition measurements in the final slab, corresponding to the tundish conditions in Figure 10 a). The predictions are seen to match reasonably well for all cases. This is significant because there are no parameters remaining to adjust in the strand submodel.

The results in Figure 10 b) clearly show the important difference between centerline and surface composition. New grade penetrates deeply into the liquid cavity and contaminates the old grade along the centerline. Old grade lingers in the tundish and mold cavity to contaminate the surface composition of the new grade. This difference is particularly evident in small tundish, thick-mold operations, where mixing in the strand is dominant.

The MIX1D model has been enhanced to act as an on-line tool by outputting the critical distances which define the length of intermixed steel product which falls outside the given composition specifications for the old and new grades. This model is currently in use at several steel

companies. In addition, it has been applied to perform parametric studies to evaluate the relative effects on the amount of intermixed steel for different intermixing operations [34] and for different operating conditions using a standard ladle-exchange operation [36].

IX. Solidification and Mold Heat Transfer

Heat transfer in the mold region of a continuous caster is controlled primarily by heat conduction across the interface between the mold the solidifying steel shell. Over most of the wide face in the mold, the interface consists of thin solid and liquid layers of mold flux of varying thicknesses. Heat transfer is determined greatly by the factors that control these thicknesses, (such as feeding events at the meniscus, flux viscosity, strength, and shell surface uniformity), the thermal conduction and radiation properties of the mold flux layers, and the contact resistances.

Many models have been developed to predict shell solidification in continuous casting. One such model, CON1D, couples a 1-D transient solidification model of the shell with a 2-D steady-state heat conduction model of the mold. It features a detailed treatment of the interface, including heat, mass, and momentum balances on the flux in the gap and the effect of oscillation marks on heat flow and flux consumption [37, 38]. Axial heat conduction can be ignored in models of steel continuous casting because it is small relative to axial advection, as indicated by the small Peclet number (casting-speed multiplied by shell thickness divided by thermal diffusivity).

Typical boundary conditions acting on the shell in the mold region are presented in Figure 11. Heat transfer to the gap is greatest at the meniscus, where the shell is thin and its thermal resistance is small. Delivery of superheat from the liquid is greatest near mold exit, where the hot turbulent jet of molten steel impinges on the solidification front. The model incorporates the superheat effect using a data base of heat flux results calculated from the turbulent fluid flow model of the liquid pool [23].

Figure 12 schematically shows the temperature and velocity distributions that arise across the interface [37]. The steep temperature gradients are roughly linear across each layer. Liquid flux attached to the strand, including flux trapped in the oscillation marks, moves downward at the casting speed. Solid flux is attached to the mold wall at the top. Lower down, it creeps along intermittently. For simplicity, the model assumes a constant average downward velocity of the solid flux, calibrated to be 10 - 20% of the casting speed.

This modeling tool can predict thermal behavior in the mold region of a caster as a function of design and operating variables, after calibration with mold thermocouple and breakout shell measurements from a given caster [39]. In addition to temperatures, the CON1D model also predicts important phenomena, such as the thicknesses of the solid and liquid flux layers in the gap. The complete freezing of the liquid powder in the interfacial gap generates friction and increases the likelihood of transverse crack formation. So long as a liquid slag film is present in contact with the steel shell, hydrodynamic friction forces remain fairly low, and a sound shell is more likely.

One example application of this model is the interpretation of thermocouple signals which are routinely monitored in the mold walls. Measured temperature fluctuations in the mold walls are already useful in the prediction and prevention of breakouts [40]. If better understood, patterns in the temperature signals might also be used to predict surface quality problems, which would ease the burden of surface inspection [41].

Towards this goal, the model was calibrated with thermocouple data and applied to predict shell thickness [42]. Then, the effect of local variations in oscillation mark depth were modeled using the same interface parameters [26]. Predictions for a section of shell with deep surface depressions are shown in Figure 13. The four oscillation marks in this section of shell are seen to be very wide and deep, with areas of 1.1 - 2.5 mm^2. Even filled with flux, they significantly reduce the local shell growth. Temperatures at the oscillation mark roots are predicted to increase significantly. The resulting decrease in shell thickness, relative to that predicted with no oscillation marks, is predicted to range from 0.5 to 0.9 mm over this section (6% maximum loss). These predictions almost exactly match measurements from the breakout shell, as shown in Figure 17. This match is significant because the model calibration was performed for a different average oscillation mark depth and did not consider local variations. It suggests that oscillation marks are indeed filled with flux, at least in this case. The drop in heat flux that accompanies each depression causes a corresponding drop in mold temperature as it passes by a given thermocouple location. Such a temperature disturbance displaced in time at several different thermocouples indicates the presence of a surface depression moving down the mold at the casting speed [43].

X. Thermal Mechanical Behavior of the Mold

Thermal distortion of the mold during operation is important to residual stress, residual distortion, fatigue cracks, and mold life. By affecting the internal geometry of the mold cavity, it is also important to heat transfer to the solidifying shell. To study thermal distortion of the mold, a 3-D finite element model with an elastic-plastic-creep constitutive model has been developed [44] using ABAQUS. In order to match the measured distortion, [44] the model had to incorporate all of the complex geometric features of the mold, including the four copper plates with their water slots, reinforced steel water box assemblies, and tightened bolts. Ferrostatic pressure pushes against the inside of the copper, but was found to have a negligible influence on mold distortion [44]. This pressure is balanced by mold clamping forces on the eight points joining the water chambers to the rigid steel frame. Its four-piece construction makes the slab mold behave very differently from single-piece bloom or billet molds, which have also been studied using thermal stress models [45].

Figure 14 illustrates typical temperature contours and the displaced shape calculated in one quarter of the mold under steady operating conditions [44]. The hot exterior of each copper plate attempts to expand, but is constrained by its colder interior and the cold, stiff, steel water jacket. This makes each plate bend in towards the solidifying steel. Maximum inward distortions of more than one millimeter are predicted just above the center of the mold faces, and below the location of highest temperature, which is found just below the meniscus.

The narrow face is free to rotate away from the wide face and contact only along a thin vertical line at the front corner of the hot face. This hot edge must transmit all of the clamping forces, so is prone to accelerated wear and crushing, especially during automatic width changes. If steel enters the gaps formed by this mechanism, this can lead to finning defects or even a sticker breakout. In addition, the widefaces may be gouged, leading to longitudinal cracks and other surface defects [44].

The high compressive stress due to constrained thermal expansion induces creep in the hot exterior of the copper plates which face the steel. This relaxes the stresses during operation, but allows residual tensile stress to develop during cooling. Over time, these cyclic thermal stresses and creep build up significant distortion of the mold plates. This can contribute greatly to remachining requirements and reduced mold life. A copper alloy with higher creep resistance is less prone to this problem. Under adverse conditions, this stress could lead to catastrophic fatigue fracture of the copper plates, when stress concentration initiates cracks at the water slot roots. Finally, the distortion predictions are important for heat transfer and behavior of the shell in the mold. This is because the distortion is on the same order as the shell shrinkage and

interfacial gap sizes. It should be taken into account when designing mold taper to avoid detrimental air gap formation.

The model has been applied to investigate these practical concerns by performing quantitative parametric studies on the effect of different process and mold design variables on mold temperature, distortion, creep and residual stress [44]. This type of stress model application will become more important in the future to optimize the design of the new molds being developed for continuous thin-slab and strip casting. For example, thermal distortion of the rolls during operation of a twin-roll strip caster is on the same order as the section thickness of the steel product.

XI. Thermal Mechanical Behavior of the Shell

The steel shell is prone to a variety of distortion and crack problems, owing to its creep at elevated temperature, combined with metallurgical embrittlement and thermal stress. To investigate these problems, a transient, thermal-elastic-viscoplastic finite-element model, CON2D, [46] has been developed to simulate thermal and mechanical behavior of the solidifying steel shell during continuous casting in the mold region [42]. This model tracks the behavior of a two-dimensional slice through the strand as it moves downward at the casting speed through the mold and upper spray zones. The 2-D nature of this modeling procedure makes the model ideally suited to simulate phenomena such as longitudinal cracks and depressions, when simulating a horizontal section [47]. A vertical section domain can be applied to simulate transverse phenomena [31].

The model consists of separate finite-element models of heat flow and stress generation that are step-wise coupled through the size of the interfacial gap. The heat flow model solves the 2-D transient energy equation, using a fixed Lagrangian grid of 3-node triangles. The interface heat flow parameters (including properties and thickness profiles of the solid and liquid mold flux layers in the gap) are chosen by calibrating the CON1D with plant measurements down the wide face, where ferrostatic pressure prevents air gap formation. The 1-D results are extrapolated around the mold perimeter by adding an air gap, which depends on the amount of shrinkage of the steel shell. The gap thickness is recalculated at each location and time, knowing the position of the strand surface (calculated by the stress model at the previous time step), and the position of the mold wall at that location and time.

Starting with stress-free liquid at the meniscus, the stress model calculates the evolution of stresses, strains, and displacements, by interpolating the thermal loads onto a fixed-grid mesh of 6-node triangles [48]. The loads are calculated from the heat transfer model results, and arise from both thermal and phase transformation strains. The out-of-plane z stress state is characterized by the "generalized-plane-strain" condition, which constrains the shell section to remain planar while it cools and contracts in the z direction. This allows the 2-D model to reasonably estimate the complete 3-D stress state, for the thin shells of interest in this work.

The stress calculation incorporates a temperature-dependent elastic modulus and temperature-, strain-rate-, composition-, and stress-state- dependent plastic flow due to high-temperature plastic creep. The elastic-viscoplastic constitutive equations (model III) developed by Kozlowski et al. [49] are used to describe the unified inelastic behavior of the shell at the high temperatures, low strains and low strain rates, important for continuous casting. The equations reproduce both the tensile test data measured by Wray [50] and creep curves from Suzuki et al [51] for austenite. They have been extended to model the enhanced creep rate in delta-ferrite, by matching measurements from Wray [52].

These constitutive equations are integrated using a new two-level algorithm, [53] which alternates between solutions at the local node point and the global system equations. The effects of volume changes due to temperature changes and phase transformations are included using a temperature- and grade-dependent thermal-linear-expansion function.

Intermittent contact between the shell and the mold is incorporated by imposing spring elements to restrain penetration of the shell into the mold. The shape of the rigid boundary of the water-cooled copper mold is imposed from a database of results obtained from a separate 3-D calculation of thermal distortion of the mold [54]. To extend model simulations below the mold, the shell is allowed to bulge outward only up to a maximum displacement, whose axial (z) profile is specified.

The thermal-mechanical model has been validated using analytical solutions, which is reported elsewhere [53]. The model was next compared with measurements of a breakout shell from an operating slab caster. An example of the predicted temperature contours and distorted shape of a region near the corner are compared in Figure 15. The interface heat flow parameters (including thickness profile of the solid and liquid mold flux layers) were calibrated using thermocouple measurements down the centerline of the wideface for typical conditions [42]. Thus, good agreement was expected and found in the region of good contact along the wideface, where

calibration was done. Around the perimeter, significant variation in shell thickness was predicted, due to air gap formation and non-uniform superheat dissipation.

Near the corner along the narrow face, steel shrinkage is seen to exceed the mold taper, which was insufficient. Thus, an air gap is predicted. This air gap lowers heat extraction from the shell in the off-corner region of the narrow face, where heat flow is one-dimensional. When combined with high superheat delivery from the bifurcated nozzle directed at this location, the shell growth is greatly reduced locally. Just below the mold, this thin region along the off-corner narrow-face shell caused the breakout.

Near the center of the narrow face, creep of the shell under ferrostatic pressure from the liquid is seen to maintain contact with the mold, so much less thinning is observed. The surprisingly close match with measurements all around the mold perimeter tends to validate the features and assumptions of the model. It also illustrates the tremendous effect that superheat has on slowing shell growth, if (and only if!) there is a gap present, which lowers heat flow.

This model has been applied to predict ideal mold taper, [55] to prevent breakouts such as the one discussed here [56] and to understand the cause of other problems such as off-corner surface depressions and longitudinal cracks in slabs [25].

A. Longitudinal Surface depressions

One of the quality problems which can affect any steel grade is the formation of longitudinal surface depressions, 2 to 8 mm deep, just off the corners along the wide faces of conventionally-cast slabs. These “gutters” are usually accompanied by longitudinal subsurface cracks and by bulging along the narrow face. Gutters are a costly problem for 304 stainless steel slabs, because the surface must be ground flat in order to avoid slivers and other defects after subsequent reheating and rolling operations.

Simulations were performed for a 203 x 914 mm stainless steel strand cast through a 810 mm long mold at 16.9 mm/s with 25 ˚C superheat, and no wide face taper [25]. Results in the mold revealed that away from the corners, ferrostatic pressure maintains good contact between the shell and the mold walls. However, “hot spots” are predicted to develop on the off-corner regions of the shell surface in the mold, as shown in both Figure 15 (narrow face) and in Figure 16 (wide face).

The hot spot on the wide face is predicted in Figure 16 to reach several hundred degrees in extreme cases, and has been reported previously. [57, 58] It may arise in several different ways. The typical lack of taper on the wide face creates an inherent tendency to form a gap between the shell and mold wide face in the off-corner region. Thermal distortion tends to bend the mold walls away from the shell [44]. Insufficient taper of the narrow face mold walls may cause the solidified corner to rotate inside the mold, lifting the shell slightly away from the off-corner mold wall [59]. Finally, excessive taper of the narrow face mold walls may compress the wide face shell, causing it to buckle at its weakest point: the thin shell at the off-corner region [59]. With large enough taper, this mechanism alone could create gutters, entirely within the mold [59, 60].

Although a thin (about 0.2 mm) gap may form in several different ways, it becomes critical only if it is filled with air. This can happen if the mold flux solidifies completely part way down the mold. It is even more likely when there are problems with flux feeding at the meniscus. Thus, mold flow issues, discussed earlier, can contribute to the hot spots. The accompanying lack of heat flow causes thinning of the shell, which is compounded by the high superheat delivered to the inside of the shell by the impinging jet in this region. The thinner shell in the off-corner region is the critical step needed to cause bending of the shell below the mold, leading to off-corner depressions.

Continuing the model simulations below the mold revealed how longitudinal off-corner depressions form when the shell at the off-corner region was thin at mold exit. Figure 16 shows the steps that occur below the mold, assuming uniform narrow-face growth, achieved from a high 1.35%/m narrow-face taper. No depression is predicted at mold exit (0.8m below meniscus). In order to observe the effect of the bulging over only two roll spacings, the specified bulging displacements (3 mm maximum) were much larger than those normally encountered (less than 0.5 mm).

Bulging between mold exit and the first support roll (reaching a first maximum peak at 0.90m below the meniscus) causes the weak off-corner region to bend and curve away from the cold, rigid corner. Then, passing beneath the first support roll (0.96m) bends the wide face back into alignment with the corner. Due to permanent creep strain, the curvature remains, in the form of a longitudinal depression. At the same time, the rotation of the rigid corner causes the narrow face to bend outward, which is observed in practice [25]. High subsurface tension is generated beneath the depression, leading to subsurface cracks in crack-sensitive steel grades.

The maximum depth of the calculated gutter after the first roll is 2 mm, growing to 3 mm at the second roll. The calculated shape corresponds to the location of the thin spot. It roughly matches the observed surface profile, as seen in Figure 17. Passing beneath each subsequent support roll causes the depression to deepen, but by lessening amounts. This continues for several more rolls, until solidification evens out the shell thickness, and the shell becomes strong enough to avoid further permanent curvature.

Other model simulations that assumed uniform heat transfer and shell growth along the wide face prior to mold exit never produced any longitudinal depressions. This suggests that solutions to the problem should focus on achieving uniform heat transfer in the mold, even though the depressions mainly form below the mold. Ensuring adequate spray cooling and proper alignment and minimum spacing of rolls to minimize the bulging below the mold is also beneficial. The effect of important casting variables on longitudinal depressions and solutions to the problem that have been achieved in practice are explained in the light of this mechanism [25].

B. Crack prediction

Continuous-cast steel is subject to a variety of different surface and subsurface cracks. Using a thermal stress model to investigate crack formation requires a valid fracture criterion, linking the calculated mechanical behavior with the microstructural phenomena that control crack initiation and propagation. The task is difficult because crack formation depends on phenomena not included in a stress model, such as microstructure, grain size and segregation. Thus, experiments are needed to determine the fracture criteria empirically.

Many of the cracks that occur during solidification are hot tears. These cracks grow between dendrites when tensile stress is imposed across barely-solidified grains while a thin film of liquid metal still coats them. Very small strains can start hot tears when the liquid film is not thick enough to permit feeding of surrounding liquid through the secondary dendrite arms to fill the gaps. Long, thin, columnar grains and alloys with a wide freezing range are naturally most susceptible. The phenomenon is worsened by microsegregation of impurities to the grain boundaries, which lowers the solidus temperature locally and complicates the calculations.

Crack formation in the shell is being investigated using the CON2D thermal stress model [61]. Figure 18 presents sample distributions of temperature, stress, and strain through the thickness of the shell, for a 0.1%C steel after 5s of solidification below the meniscus. To minimize numerical

errors, a very fine, graded mesh was required, including 201 nodes per row across the 20 mm-thick domain. The time step increases from 0.001s initially to 0.005s at 1s.

The temperature profile is almost linear across the 6-mm thick shell in Figure 18 a), with a mushy zone (liquid and delta-ferrite) that is 1.4 mm thick (33 ˚C). The stress profile shows that the slab surface is in compression. This is because, in the absence of friction with the mold, the surface layer solidifies and cools stress free. As each inner layer solidifies, it cools and tries to shrink, while the surface temperature remains relatively constant. The slab is constrained to remain planar, so complementary subsurface tension and surface compression stresses are produced. To maintain force equilibrium, note that the average stress through the shell thickness is zero. It is significant that the maximum tensile stress of about 4 MPa is found near the solidification front. This generic subsurface tensile stress is responsible for hot tear cracks, when accompanied by metallurgical embrittlement.

Although it has no effect on stress, the model tracks strain in the liquid. When liquid is present, fluid flow is assumed to occur in order to exactly match the shrinkage. A finite element is treated as liquid in this model when any node in the element is above the specified coherency temperature (set to the solidus). These liquid elements are set to have no elastic strain, and consequently develop no stress. The difference between the total strain and thermal strain in liquid elements is assumed to be made up by a “flow strain”. This method allows easy tracking of various fracture criteria. For example, a large flow strain when the solid fraction is high indicates high cracking potential. It is also needed for future macrosegregation calculations.

Typical strain distributions are shown in Figure 18 b) for 0.1%C steel. At the surface, the inelastic and elastic strains are relatively small, so the total strain matches the thermal strain accumulated in the solid. Ideal taper calculations can therefore be crudely estimated based solely on the temperature of the surface. At the solidification front, liquid contraction exceeds solid shell shrinkage, causing flow into the mushy zone. It may be significant that 0.1% inelastic strain is accumulated in the solid during the δ to γ transformation. This occurs within the critical temperature range 20-60 ˚C below the solidus, where segregation can embrittle the grain boundaries, liquid feeding is difficult, and strain can concentrate in the thin liquid films. However, the model predictions are less than the measured values needed to form cracks using either critical stress [62], or critical strain [63] criteria. Thus, other unmodeled phenomena are surely important.

Longitudinal surface cracks might initiate within 1 second of the meniscus if the shell sticks to the mold. After this time, the shell is able to withstand the ferrostatic pressure and should contract to break away any sticking forces. This creates non-uniform surface roughness, however, which leads to local variations in heat transfer and shell growth rate. Strain concentrates in the hotter, thinner shell at the low heat flux regions. Strain localization may occur on both the small scale (when residual elements segregate to the grain boundaries) and on a larger scale (within surface depressions or hot spots). Later sources of tensile stress (including constraint due to sticking, unsteady cooling below the mold, bulging, and withdrawal) worsen strain concentration and promote crack growth. Further work is needed to investigate these phenomena.

XII. Future Frontiers

This paper has shown several examples of the application of mathematical models to quantifying and understanding the mechanisms of defect formation during the continuous casting of steel slabs. Significant gains have been made in recent years. Despite the sophistication of existing models, much more work is needed to quantify, incorporate, and simplify the key phenomena into better models before the use of mathematical modeling tools to design process improvements reaches its full potential and usefulness.

The emerging continuous casting processes, such as thin slab and strip casting, present several special challenges, which offer opportunities for the application of modeling tools. Reducing the strand thickness from 8 inches to 2-4 inches requires higher casting speeds, if productivity is to be matched. When combined with the thinner mold, these processes are more prone to the fluid flow problems discussed in this chapter. Thinner product (with more surface) puts more demand on solving surface quality problems. Mold distortion is a greater concern, both because it is relatively larger for the thinner product, and because mold life is more critical for the expensive molds needed in these processes. The integration of casting and deformation processing together requires better understanding of the interaction between microstructure, properties, and processing. Conventional slab casting has had three decades of development and is still not perfected. For these new processes to thrive, the learning curve towards process optimization to produce quality steel needs to be shorter [64].

As computer hardware and software continue to improve, mathematical models will grow in importance as tools to meet these challenges. By striving towards more comprehensive mechanistic models, better understanding and process improvements may be possible.

Acknowledgments

The author wishes to thank the member companies of the Continuous Casting Consortium at UIUC for the many years of support which has made this work possible and the National Center for Supercomputing Applications (NCSA) at UIUC for computing time. Special thanks are extended to the many excellent graduate students and research associates supported by the CCC who performed the years of hard work referenced here.

Figure Caption List

Fig. 1. Schematic of steel continuous casting process

Fig. 2. Schematic of phenomena in the mold region

Fig. 3. Flow pattern in nozzle with slide gate [3]
a) Velocities with 10% volume fraction argon injection
b) Gas fraction (lighter areas have more argon)

Fig. 4. Flow pattern in SEN with 15˚ up-angled nozzle ports [7]
a) Closeup of 3-D velocities near port
b) View looking into port showing swirl

Fig. 5. Flow pattern in slab casting mold showing effect of argon gas on top surface velocities [28]
a) without gas
b) with gas

Fig. 6 Superheat temperature distribution in mold [28] compared with measurements [27]

Fig. 7. Comparison between calculated turbulent kinetic energy and measured level fluctuations [20]
a) Low argon fraction (high throughput)
b) High argon fraction (low throughput)

Fig. 8. Comparison of measured and predicted melt-interface positions [32]

Fig. 9 Sample trajectories of five 208-micron solid alumina inclusion particles [3]

Fig. 10 Predicted intermixing during a grade change compared with experiments [34]
a) Composition history exiting tundish into mold
b) Composition distribution in final solid slab

Fig. 11 Typical isotherms and boundary conditions calculated on shell solidifying in mold [65]

Fig. 12 Velocity and temperature profiles across interfacial gap layers (no air gap) [38]

Fig. 13 Comparison of predicted and measured shell thickness with oscillation mark profile and surface temperatures for large, flux-filled oscillation marks [26]

Fig. 14 Distorted mold shape during operation (50X magnification) with temperature contours (˚C) [44]

Fig. 15 Comparison between predicted and measured shell thickness in a horizontal (x-y) section through the corner of a continuous-cast steel breakout shell [42]

Fig. 16 Calculated evolution of shape of shell below mold (to scale) with isotherms (˚C) [25]

Fig. 17 Comparison of calculated and measured surface shape profile across wideface, showing gutter [25]

Fig. 18 Typical Temperature, Stress, and Strain distributions through shell thickness [61]
a) stress and temperature profiles
b) strain components

References

1. W.H. Emling, T.A. Waugaman, S.L. Feldbauer, A.W. Cramb. Subsurface Mold Slag Entrainment in Ultra-Low Carbon Steels. in Steelmaking Conference Proceedings, 77, Chicago, IL: ISS, Warrendale, PA, 1994, pp 371-379.

2. D.E. Hershey, B.G. Thomas and F.M. Najjar. Turbulent Flow through Bifurcated Nozzles. International Journal for Numerical Methods in Fluids, 17: 1993, pp 23-47.

3. B.G. Thomas, A. Dennisov and H. Bai. Behavior of Argon Bubbles during Continuous Casting of Steel. in Steelmaking Conference Proceedings, 80, Chicago, IL: ISS, Warrendale, PA., 1997, pp 375-384.

4. FLUENT. Report, Fluent, Inc., Lebanon, New Hampshire, 1996.

5. M. Burty. Experimental and Theoretical Analysis of Gas and Metal Flows in Submerged Entry Nozzles in Continuous Casting. in PTD Conference Proceedings, 13, Nashville, TN: ISS, Warrendale, PA, 1995, pp 287-292.

6. F.M. Najjar, B.G. Thomas and D.E. Hershey. Turbulent Flow Simulations in Bifurcated Nozzles: Effects of Design and Casting Operation. Metallurgical Transactions B, 26B: (4): 1995, pp 749-765.

7. D. Hershey. Turbulent Flow of Molten Steel through Submerged Bifurcated Nozzles in the Continuous Casting Process. Masters Thesis, University of Illinois, 1992.

8. M.S. Engleman. FIDAP. Fluid Dynamics International, Inc., 500 Davis Ave., Suite 400, Evanston, IL 60201, 1994.

9. B.G. Thomas, X. Huang and R.C. Sussman. Simulation of Argon Gas Flow Effects in a Continuous Slab Caster. Metall. Trans. B, 25B: (4): 1994, pp 527-547.

10. N. Bessho, R. Yoda, H. Yamasaki, T. Fujii, T. Nozaki, S. Takatori. Numerical Analysis of Fluid Flow in the Continuous Casting Mold by a Bubble Dispersion Model. Iron Steelmaker, 18: (4): 1991, pp 39-44.

11. K. Takatani, K. Nakai, N. Kasai, T. Watanabe, H. Nakajima. Analysis of Heat Transfer and Fluid Flow in the Continuous Casting Mold with Electromagnetic Brake. ISIJ International, 29: (12): 1989, pp 1063-1068.

12. P. Gardin, J.Galpin, M. Regnier, J. Radot. Liquid Steel Flow Control inside Continuous Casting Mold using a static magnetic field. IEEE Trans. on Magnetics, 31: (3): 1995, pp 2088-2091.

13. M. Zeze, H. Tanaka, E. Takeuchi, S. Mizoguchi. Continuous Casting of Clad Steel Slab with Level Magnetic Field Brake. in Steelmaking Conference Proceedings, 79, Pittsburgh, PA: ISS, Warrendale, PA, 1996, pp 225-230.

14. A. Idogawa, M. Sugizawa, S. Takeuchi, K. Sorimachi, T. Fujii. Control of molten steel flow in continuous casting mold by two static magnetic fields imposed on whole width. Mat. Sci. & Eng., A173: 1993, pp 293-297.

15. N. Saluja, O.J. Ilegbusi and J. Szekely. Three-dimensional Flow and Free Surface Phenomena in Electromagnetically Stirred Molds in Continuous Casting. in Proc Sixth Internat. Iron Steel Congress, 4, Nagoya, JP: ISIJ, Tokyo, 1990, pp 338-346.

16. Y. Kishida, K. Takeda, I. Miyoshino, E. Takeuchi. Anisotropic Effect of Magnetohydrodynamics on Metal Solidification. ISIJ International, 30: (1): 1990, pp 34-40.

17. J.P. Birat and J. Chone. Electromagnetic stirring on billet, bloom, and slab continuous casters: state of the art in 1982. Ironmaking and Steelmaking, 10: (6): 1983, pp 269-281.

18. D. Gupta and A.K. Lahiri. A Water Model Study of the Flow Asymmetry Inside a Continuous Slab Casting Mold. Metallurgical and Materials Transactions, 27B: (5): 1996, pp 757-764.

19. T. Honeyands and J. Herbertson. Flow Dynamics in Thin Slab Caster Moulds. Steel Research, 66: (7): 1995, pp 287-293.

20. X. Huang and B.G. Thomas. Modeling Transient Flow Phenomena in Continuous Casting of Steel. in 35th Conference of Metallurgists, 23B, C. Twigge-Molecey, eds., Montreal, Canada: CIM, 1996, pp 339-356.

21. B.M. Gebert, M.R. Davidson and M.J. Rudman. Calculated Oscillations of a Confined Submerged Liquid Jet. in Inter Conf on CFD in Mineral & Metal Processing and Power Generation, M.P. Schwarz, eds., Melbourne, Australia: CSIRO, 1997, pp 411-417.

22. J. Herbertson, O.L. He, P.J. Flint, R.B. Mahapatra. in 74th Steelmaking Conference Proceedings, 74, ISS, Warrendale, PA, 1991, pp 171-185.

23. X. Huang, B.G. Thomas and F.M. Najjar. Modeling Superheat Removal during Continuous Casting of Steel Slabs. Metallurgical Transactions B, 23B: (6): 1992, pp 339-356.

24. B.G. Thomas and F.M. Najjar. Finite-Element Modeling of Turbulent Fluid Flow and Heat Transfer in Continuous Casting. Applied Mathematical Modeling, 15: 1991, pp 226-243.

25. B.G. Thomas, A. Moitra and R. McDavid. Simulation of Longitudinal Off-Corner Depressions in Continuously-Cast Steel Slabs. ISS Transactions, 23: (4): 1996, pp 57-70.

26. B.G. Thomas, D. Lui and B. Ho. Effect of Transverse and Oscillation Marks on Heat Transfer in the Continuous Casting Mold. in Applications of Sensors in Materials Processing, V. Viswanathan, eds., Orlando, FL: TMS, Warrendale, PA, 1997, pp 117-142.

27. C. Offerman. Internal Structure in Continuously Cast Slabs by the Metal Flow in the Mould. Scandanavian J. Metallurgy, 10: 1981, pp 25-28.

28. X. Huang and B.G. Thomas. unpublished research. Report, University of Illinois, 1996.

29. G.A. Panaras, A. Theodorakakos and G. Bergeles. Numerical Investigation of the Free Surface in a continuous Steel Casting Mold Model. Dept. of Mech. Eng., N.T.U.A., Athens, Greece, unpublished research, 1997.

30. T. Teshima, M. Osame, K. Okimoto, Y. Nimura. Improvements of surface property of steel at high casting speed. in Steelmaking Conference Proceedings, 71, Warrendale, PA: Iron & Steel Society, 1988, pp 111-118.

31. B.G. Thomas and H. Zhu. Thermal Distortion of Solidifying Shell in Continuous Casting of Steel. in Proceedings of Internat. Symposia on Advanced Materials & Tech. for 21st Century, I. Ohnaka and D. Stefanescu, eds., Honolulu, HI: TMS, Warrendale, PA, 1996, pp 197-208.

32. R. McDavid and B.G. Thomas. Flow and Thermal Behavior of the Top-Surface Flux/ Powder Layers in Continuous Casting Molds. Metallurgical Transactions B, 27B: (4): 1996, pp 672-685.

33. Y. Miki, B.G. Thomas, A. Denissov, Y. Shimada. Model of Inclusion Removal During RH Degassing of Steel. Iron and Steelmaker, 24: (8): 1997, pp 31-38.

34. X. Huang and B.G. Thomas. Intermixing Model of Continuous Casting During a Grade Transition. Metallurgical Transactions B, 27B: (4): 1996, pp 617-632.

35. X. Huang and B.G. Thomas. Modeling of Steel Grade Transition in Continuous Slab Casting Processes. Metallurgical Transactions, 24B: 1993, pp 379-393.

36. B.G. Thomas. Modeling Study of Intermixing in Tundish and Strand during a Continuous-Casting Grade Transition. ISS Transactions, 24: (12): 1996, pp 83-96.

37. B. Ho. Characterization of Interfacial Heat Transfer in the Continuous Slab Casting Process. Masters Thesis, University of Illinois at Urbana-Champaign, 1992.

38. B.G. Thomas, B. Ho and G. Li. CON1D User's Manual. Report, University of Illinois, 1994.

39. B.G. Thomas and B. Ho. Spread Sheet Model of Continuous Casting. J. Engineering Industry, 118: (1): 1996, pp 37-44.

40. W.H. Emling and S. Dawson. Mold Instrumentation for Breakout Detection and Control. in Steelmaking Conference Proceedings, 74, Warrendale, PA: Iron and Steel Society, 1991, pp 197-217.

41. J.K. Brimacombe. Empowerment with Knowledge - toward the Intelligent Mold for the Continuous Casting of Steel Billets. Metallurgical Transactions B, 24B: 1993, pp 917-935.

42. A. Moitra and B.G. Thomas. Application of a Thermo-Mechanical Finite Element Model of Steel Shell Behavior in the Continuous Slab Casting Mold. in Steelmaking Proceedings, 76, Dallas, TX: Iron and Steel Society, 1993, pp 657-667.

43. M.S. Jenkins, B.G. Thomas, W.C. Chen, R.B. Mahapatra. Investigation of Strand Surface Defects using Mold Instrumentation and Modelling. in Steelmaking Conference Proceedings, 77, Warrendale, PA: Iron and Steel Society, 1994, pp 337-345.

44. B.G. Thomas, G. Li, A. Moitra, D. Habing. Analysis of Thermal and Mechanical Behavior of Copper Molds during Continuous Casting of Steel Slabs. Iron and Steelmaker (ISS Transactions), 25: (10): 1998, pp 125-143.

45. I.V. Samarasekera, D.L. Anderson and J.K. Brimacombe. The Thermal Distortion of Continuous Casting Billet Molds. Metallurgical Transactions B, 13B: (March): 1982, pp 91-104.

46. A. Moitra, B.G. Thomas and W. Storkman. Thermo-mechanical model of Steel Shell Behavior in the Continuous Casting Mold. Proceedings of TMS Annual Meeting, San Diego, CA, 1992, The Minerals, Metals, and Materials Society, Warrendale, PA.

47. A. Moitra. Thermo-mechanical model of Steel Shell Behavior in Continuous Casting. Ph.D. Thesis, University of Illinois at Urbana-Champaign, 1993.

48. H. Zhu. Coupled Thermal-Mechanical Fixed-Grid Finite-Element Model with Application to Initial Solidification. PhD Thesis, University of Illinois, 1997.

49. P. Kozlowski, B.G. Thomas, J. Azzi, H. Wang. Simple Constitutive Equations for Steel at High Temperature. Metallurgical Transactions A, 23A: (March): 1992, pp 903-918.

50. P.J. Wray. Effect of Carbon Content on the Plastic Flow of Plain Carbon Steels at Elevated Temperatures. Metallurgical Transactions A, 13A: (1): 1982, pp 125-134.

51. T. Suzuki, K.H. Tacke, K. Wunnenberg, K. Schwerdtfeger. Creep Properties of Steel at Continuous Casting Temperatures. Ironmaking and Steelmaking, 15: (2): 1988, pp 90-100.

52. P.J. Wray. Plastic Deformation of Delta-Ferritic Iron at Intermediate Strain Rates. 7A: (Nov.): 1976, pp 1621-1627.

53. H. Zhu and B.G. Thomas. Evaluation of Finite Element Methods for Simulation of Stresses During Solidification. Report, University of Illinois, 1994.

54. B.G. Thomas, A. Moitra, D.J. Habing, J.A. Azzi. A Finite Element Model for Thermal Distortion of Continuous Slab Casting Molds. Proceedings of the 1st European Conference on Continuous Casting, Florence, Italy, 1991, Associazione Italiana di Metallurgia, 2, pp 2.417-2.426.

55. B.G. Thomas, A. Moitra and W.R. Storkman. Optimizing Taper in Continuous Slab Casting Molds Using Mathematical Models. in Proceedings, 6th International Iron and Steel Congress, 3, Nagoya, Japan: Iron & Steel Inst. Japan, Tokyo, 1990, pp 348-355.

56. G.D. Lawson, S.C. Sander, W.H. Emling, A. Moitra, B.G. Thomas. Prevention of Shell Thinning Breakouts Associated with Widening Width Changes. in Steelmaking Conference Proceedings, 77, Warrendale, PA: Iron and Steel Society, 1994, pp 329-336.

57. K. Kinoshita, H. Kitaoka and T. Emi. Influence of Casting Conditions on the Solidification of Steel Melt in Continuous Casting Mold. Tetsu-to-Hagane, 67: (1): 1981, pp 93-102.

58. K. Sorimachi, M. Shiraishi and K. Kinoshita. Continuous Casting of High Carbon Steel Slabs at Chiba Works. 2nd Process Tech. Div. Conference, Chicago, IL, 1981, pp 188-193.

59. W.R. Storkman and B.G. Thomas. Mathematical Models of Continuous Slab Casting to Optimize Mold Taper. Modeling of Casting and Welding Processes, Palm Coast, FL, 1988, Engineering Foundation, 4, pp 287-297.

60. R.B. Mahapatra, J.K. Brimacombe and I.V. Samarasekera. Mold Behavior and its Influence on Product Quality in the Continuous Casting of Slabs: Part II. Mold Heat Transfer, Mold Flux Behavior, Formation of Oscillation Marks, Longitudinal Off-corner Depressions, and Subsurface Cracks. Metallurgical Transactions B, 22B: (December): 1991, pp 875-888.

61. B.G. Thomas and J.T. Parkman. Simulation of Thermal Mechanical Behavior during Initial Solidification. Thermec 97 Internat. Conf. on Thermomechanical Processing of Steel and Other Materials, Wollongong, Australia, 1997, TMS.

62. C. Bernhard, H. Hiebler and M. Wolf. Simulation of Shell Strength Properties by the SSCT Test. ISIJ International, 36: 1996, pp S163-S166.

63. A. Yamanaka, K. Nakajima and K. Okamura. Critical strain for internal crack formation in continuous casting. Ironmaking and Steelmaking, 22: (6): 1995, pp 508-512.

64. I.V. Samarasekera, B.G. Thomas and J.K. Brimacombe. The Frontiers of Continuous Casting. Julian Szekely Memorial Symposium on Materials Processing, M.I.T., Boston, MA., 1997, TMS, Warrendale, PA.

65. B.G. Thomas. Mathematical Modeling of the Continuous Slab Casting Mold, a State of the Art Review. in Mold Operation for Quality and Productivity, A. Cramb, eds., Iron and Steel Society: Warrendale, PA, 1991, pp 69-82.

Figure Caption List

Fig. 1. Schematic of steel continuous casting process

Fig. 2. Schematic of phenomena in the mold region

Fig. 3. Flow pattern in nozzle with slide gate [3]
a) Velocities with 10% volume fraction argon injection
b) Gas fraction (lighter areas have more argon)

Fig. 4. Flow pattern in SEN with 15˚ up-angled nozzle ports [7]
a) Closeup of 3-D velocities near port
b) View looking into port showing swirl

Fig. 5. Flow pattern in slab casting mold showing effect of argon gas on top surface velocities [28]
a) without gas
b) with gas

Fig. 6 Superheat temperature distribution in mold [28] compared with measurements [27]

Fig. 7. Comparison between calculated turbulent kinetic energy and measured level fluctuations [20]
a) Low argon fraction (high throughput)
b) High argon fraction (low throughput)

Fig. 8. Comparison of measured and predicted melt-interface positions [32]

Fig. 9 Sample trajectories of five 208-micron solid alumina inclusion particles [3]

Fig. 10 Predicted intermixing during a grade change compared with experiments [34]
a) Composition history exiting tundish into mold
b) Composition distribution in final solid slab

Fig. 11 Typical isotherms and boundary conditions calculated on shell solidifying in mold [65]

Fig. 12 Velocity and temperature profiles across interfacial gap layers (no air gap) [38]

Fig. 13 Comparison of predicted and measured shell thickness with oscillation mark profile and surface temperatures for large, flux-filled oscillation marks [26]

Fig. 14 Distorted mold shape during operation (50X magnification) with temperature contours (˚C) [44]

Fig. 15 Comparison between predicted and measured shell thickness in a horizontal (x-y) section through the corner of a continuous-cast steel breakout shell [42]

Fig. 16 Calculated evolution of shape of shell below mold (to scale) with isotherms (˚C) [25]

Fig. 17 Comparison of calculated and measured surface shape profile across wideface, showing gutter [25]

Fig. 18 Typical Temperature, Stress, and Strain distributions through shell thickness [61]
a) stress and temperature profiles
b) strain components

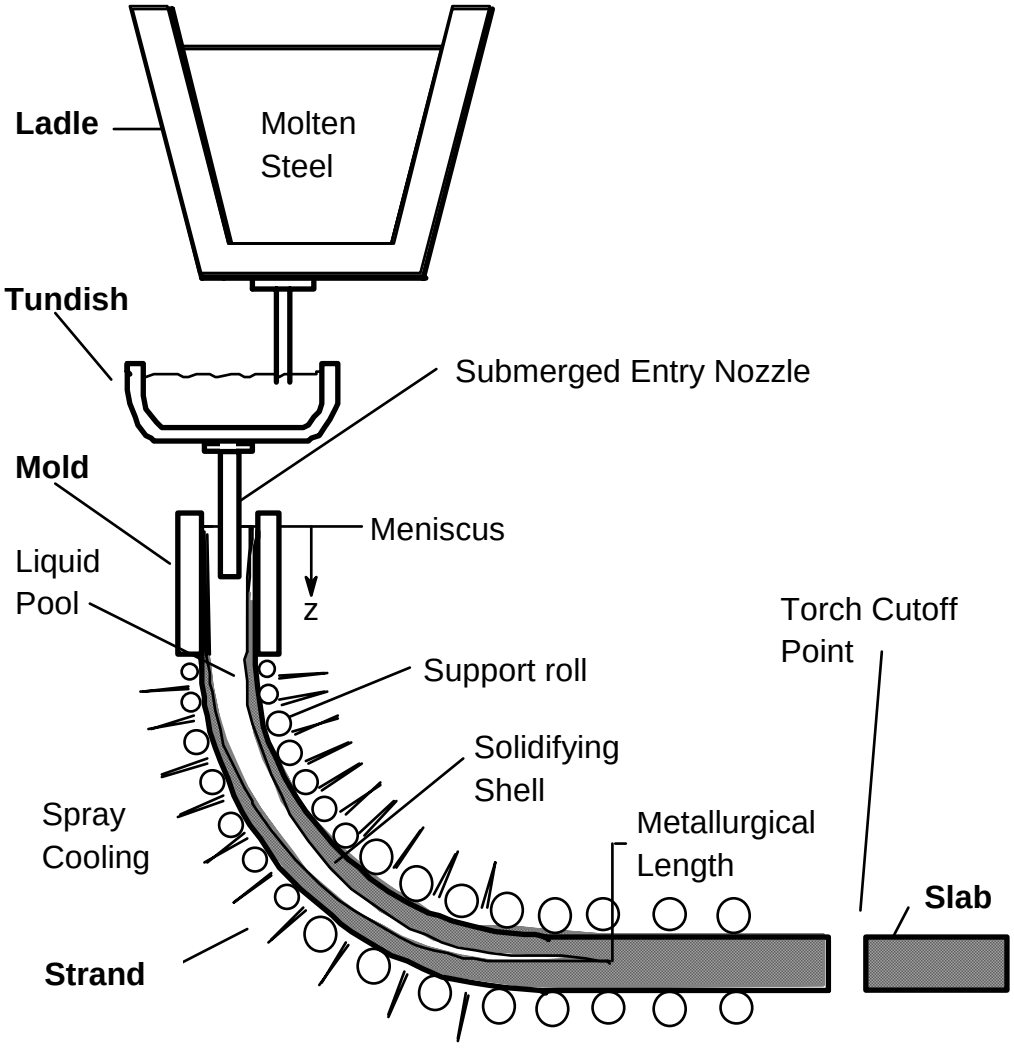

Figure 1. Schematic of steel continuous casting process

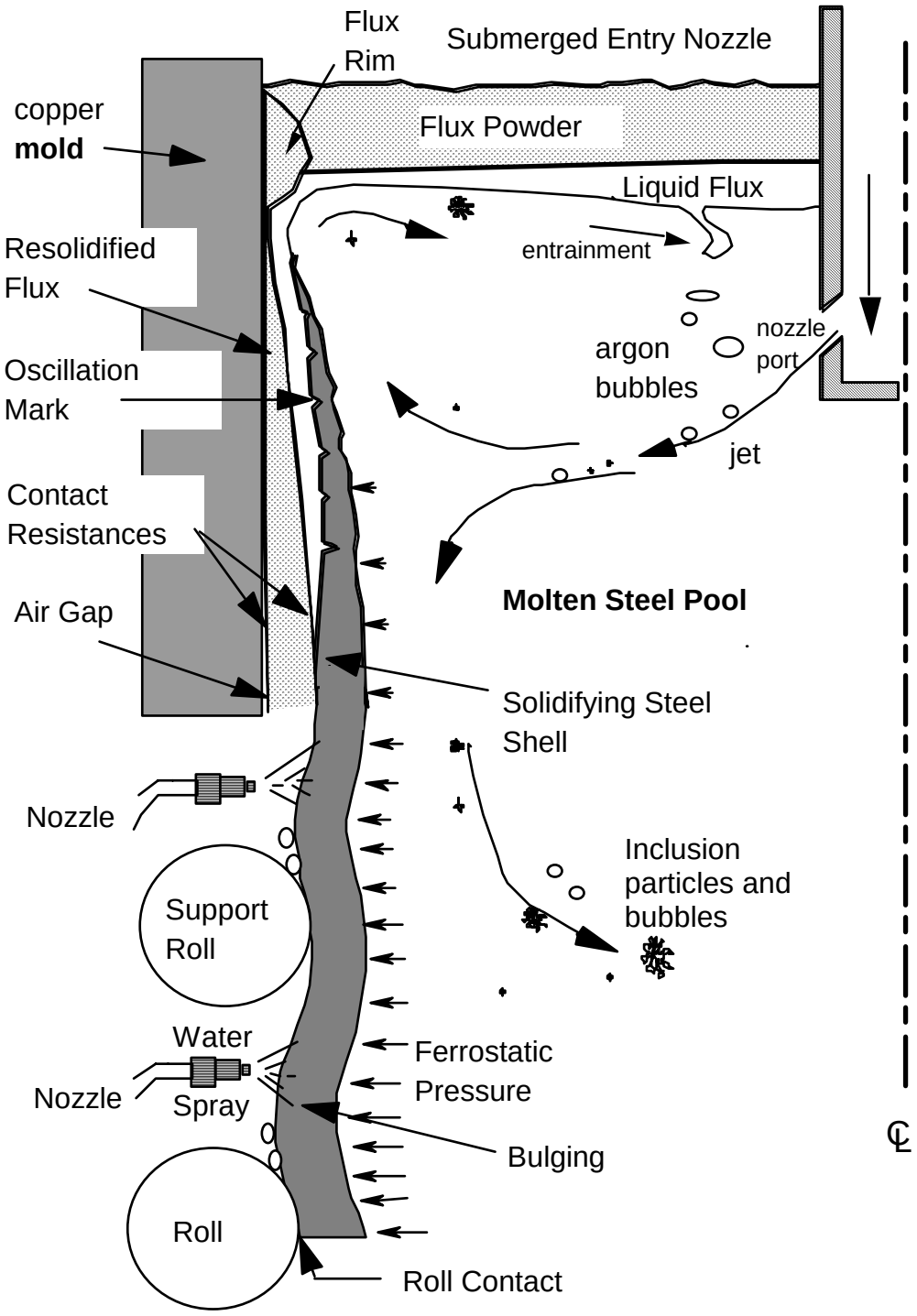

Fig. 2 Schematic of phenomena in the mold region

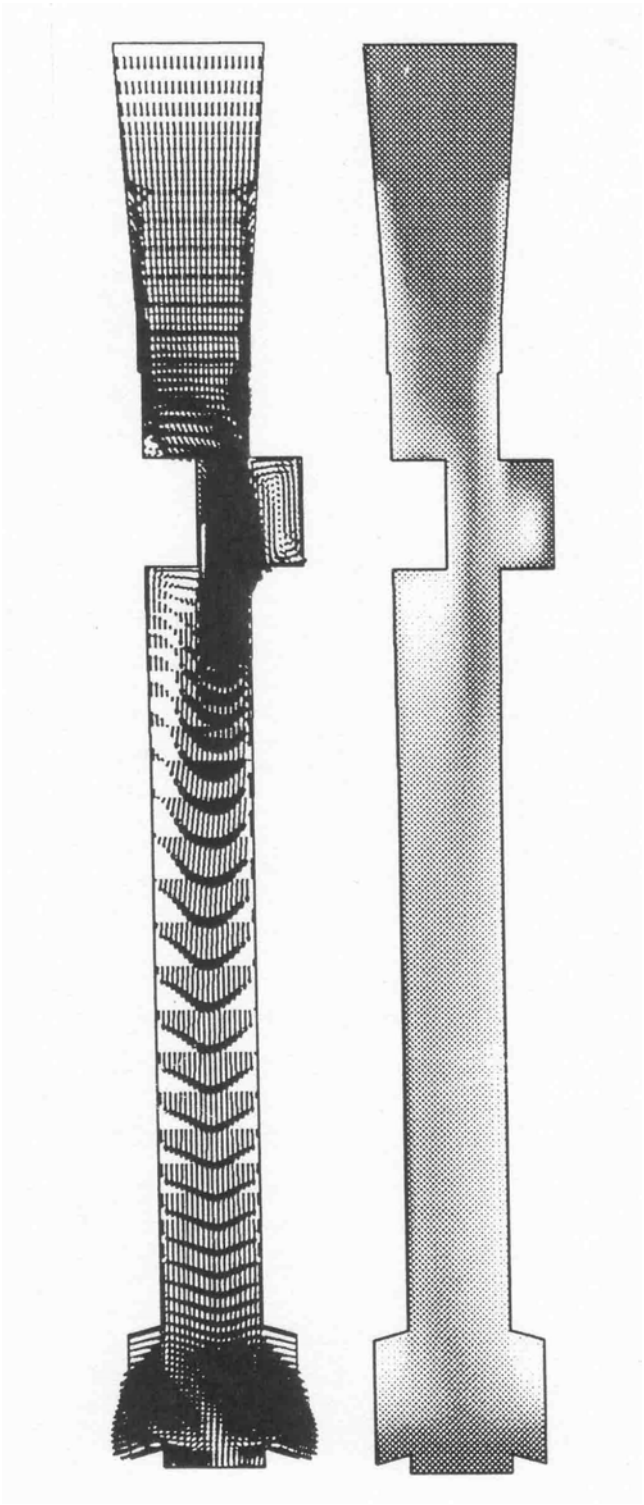

a) **b)**

Fig. 3. Flow pattern in nozzle with slide gate
a) Velocities with 10% volume fraction argon injection
b) Gas fraction (lighter areas have more argon)

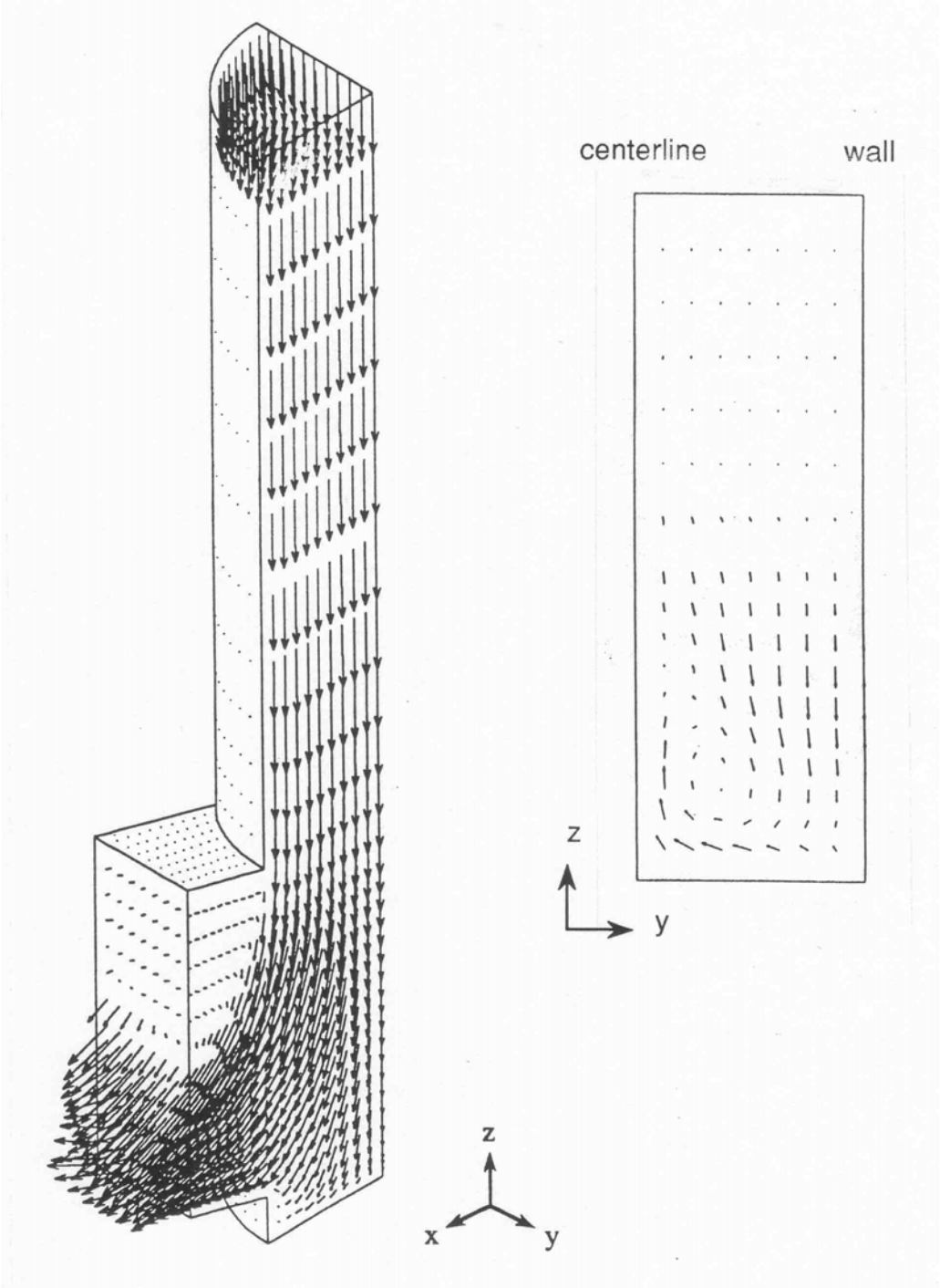

a) b)

Fig. 4. Flow pattern in SEN with 15˚ up-angled nozzle ports
a) Closeup of 3-D velocities near port
b) View looking into port showing swirl

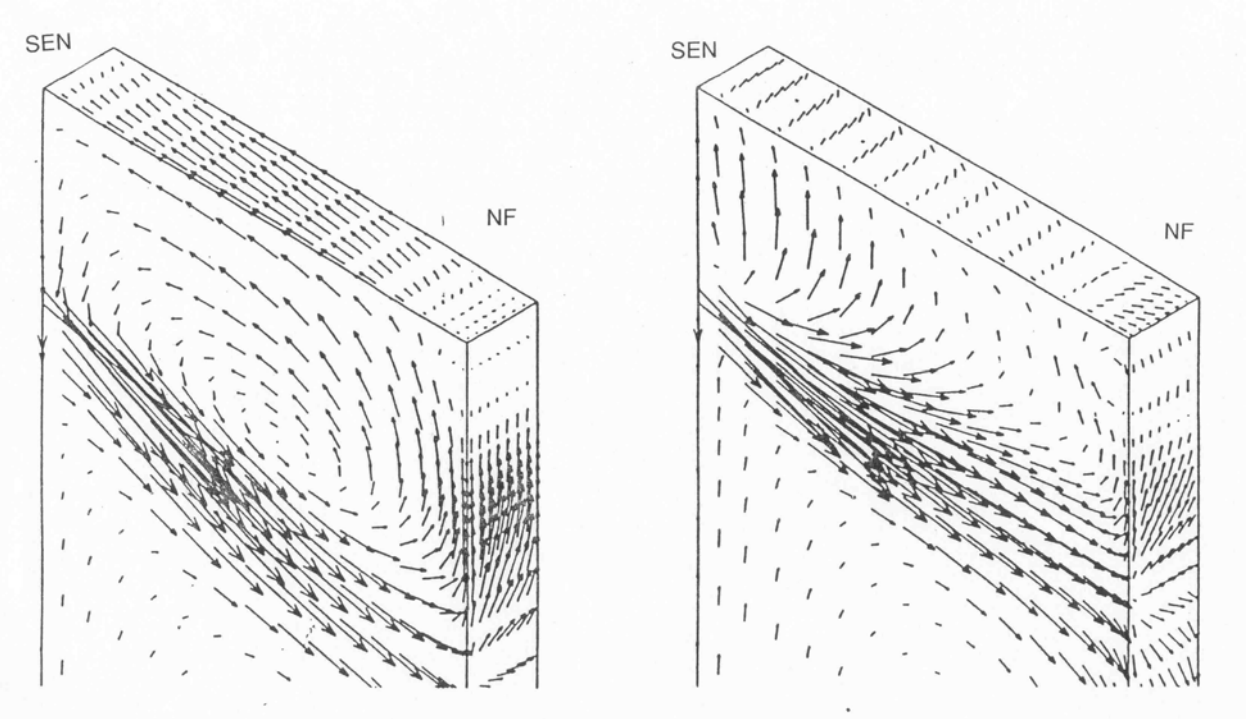

a) Without Gas **b) With Gas**

Fig. 5. Flow pattern in slab casting mold showing effect of argon gas on top surface velocities

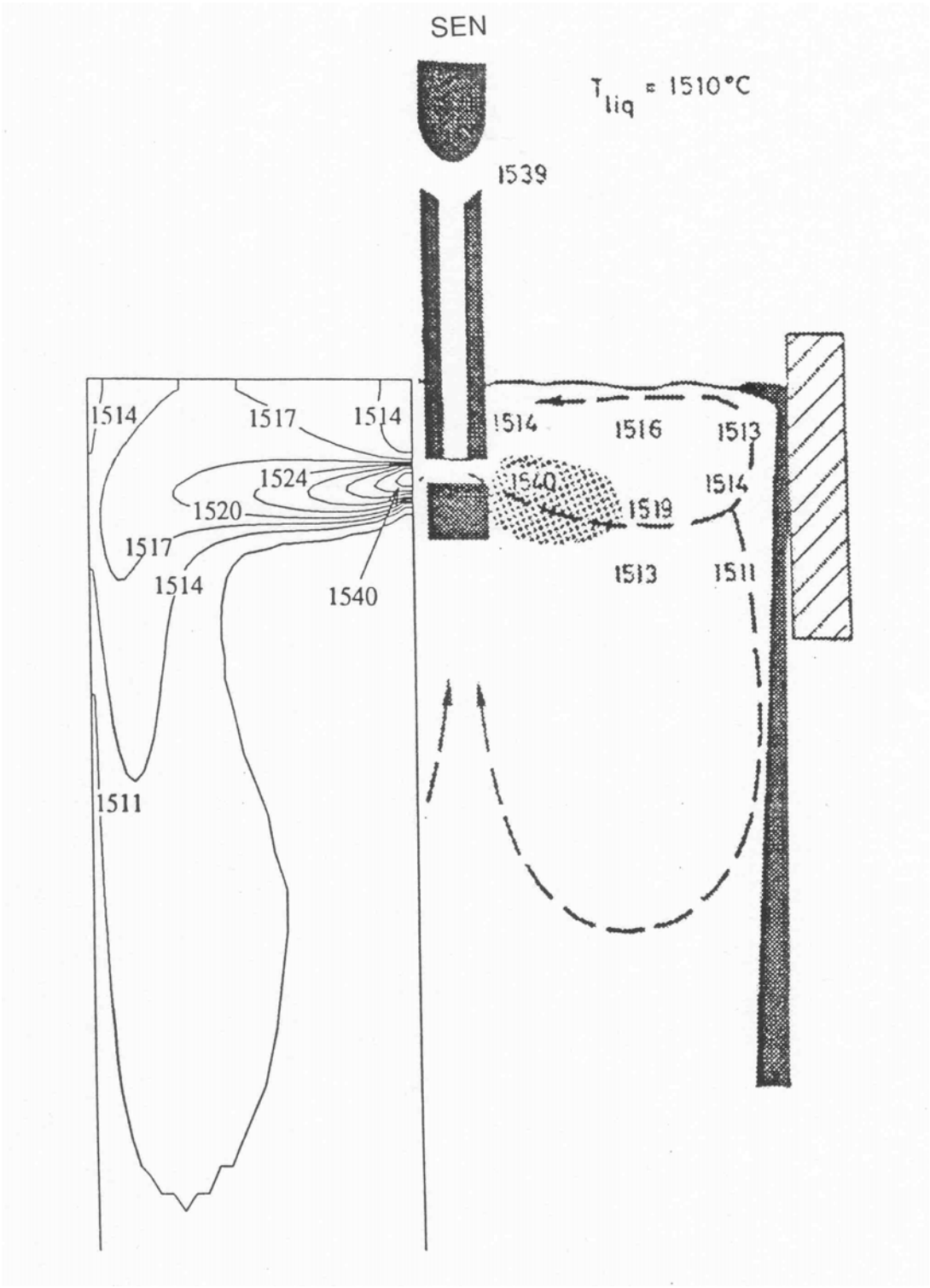

Fig. 6 Superheat temperature distribution in mold

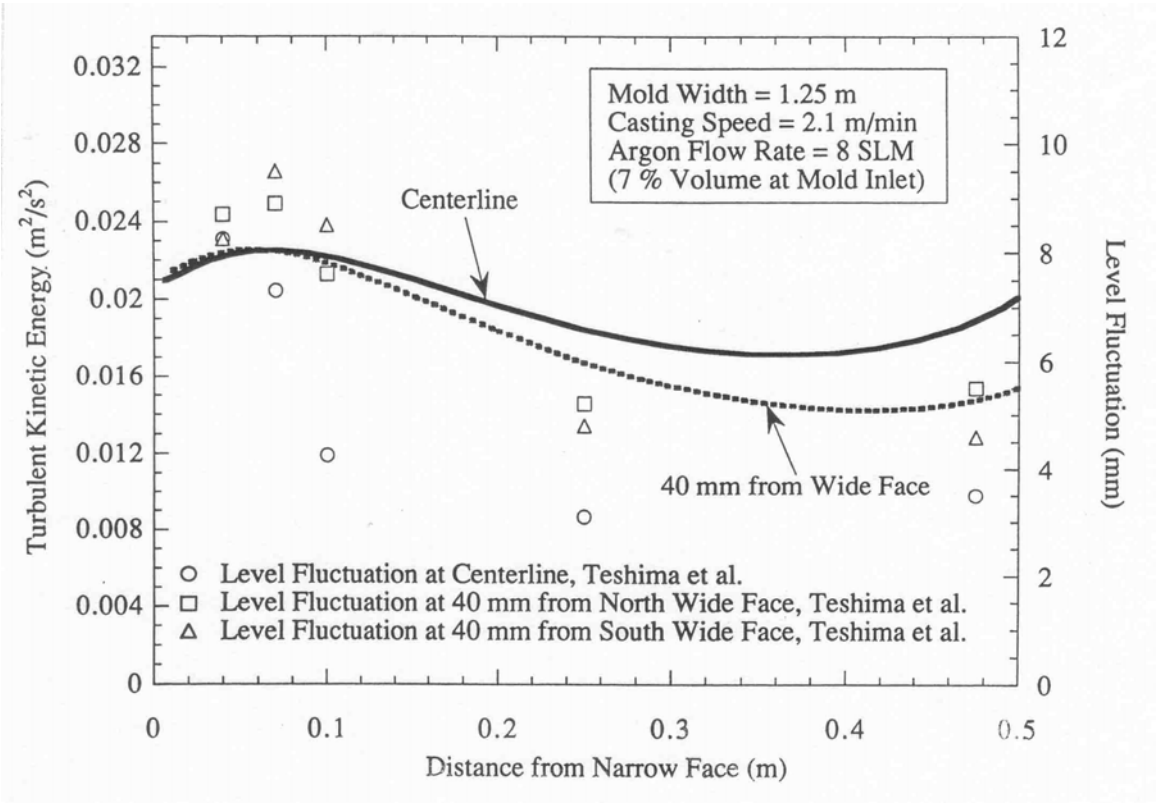

a) Low argon fraction (high throughput)

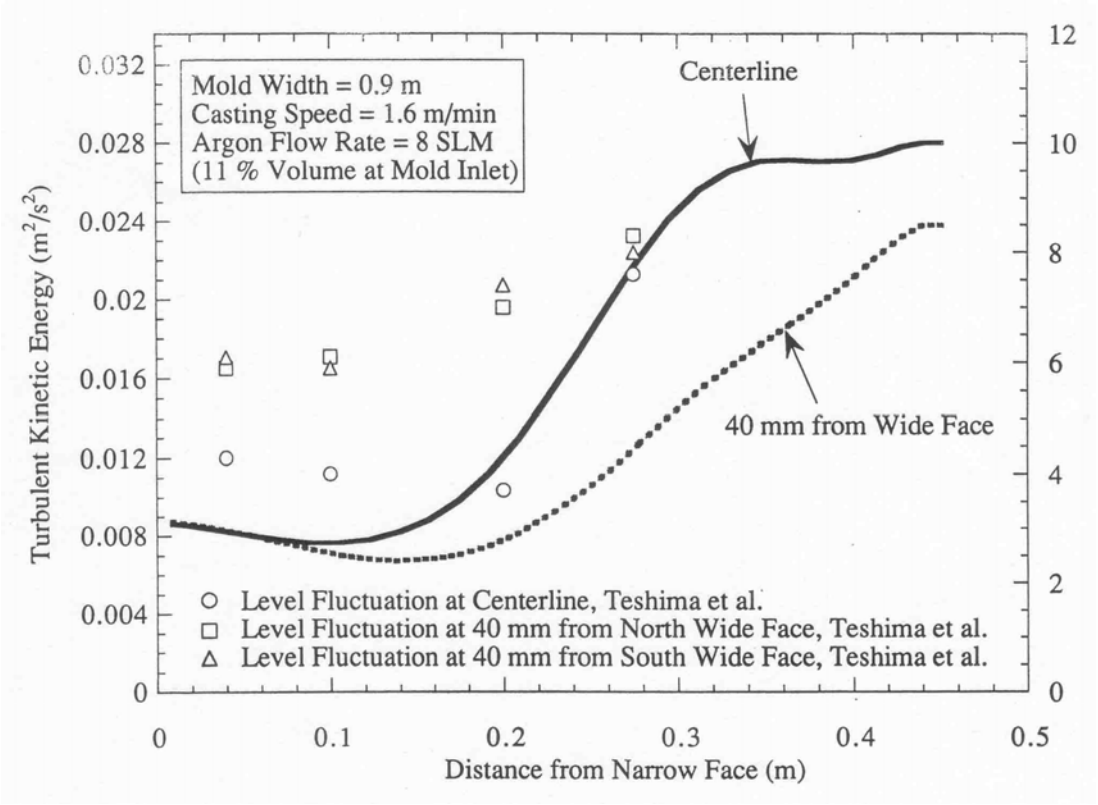

b) High argon fraction (low throughput)

Figure 7. Comparison between calculated turbulent energy and measured level fluctuations

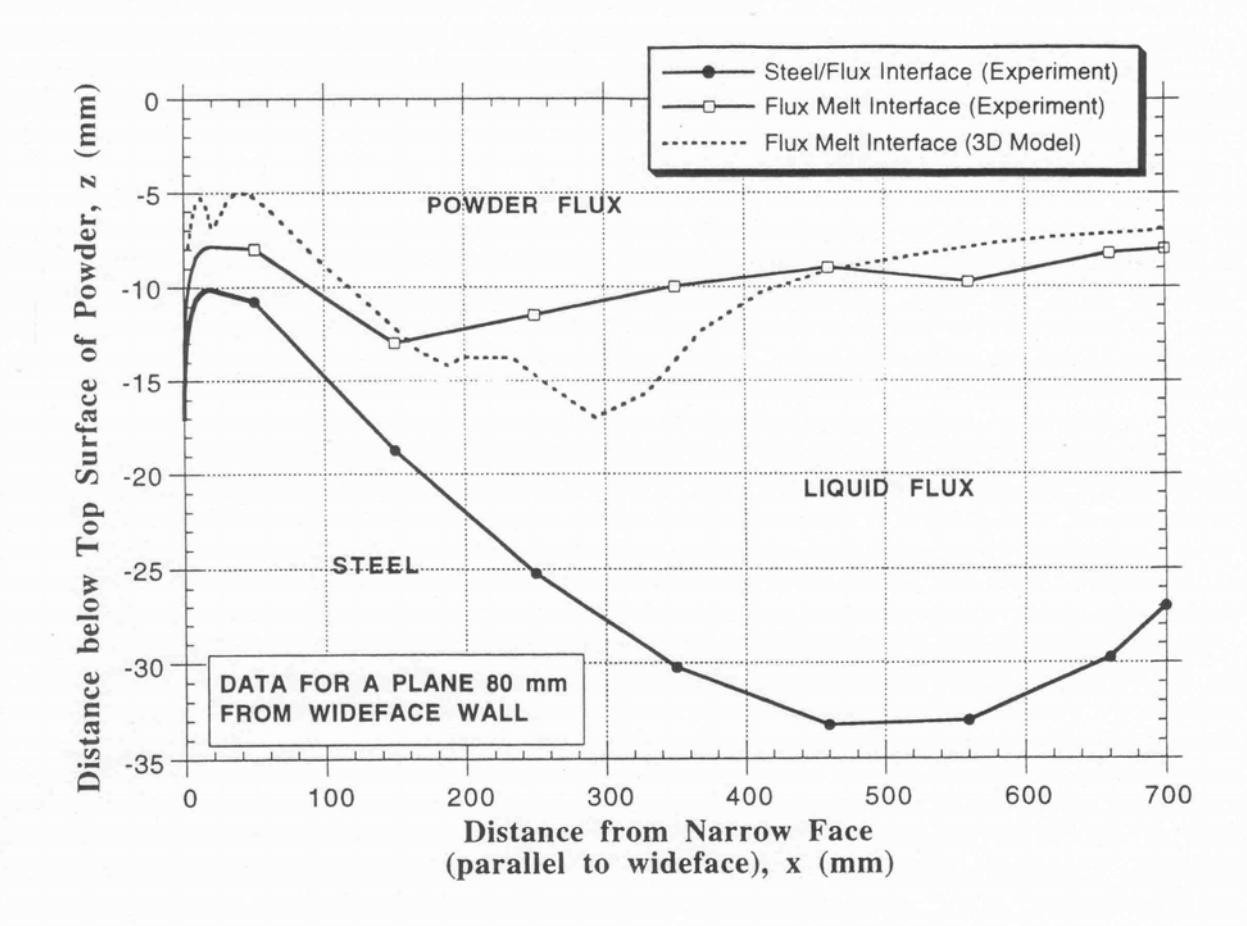

Fig. 8. Comparison of measured and predicted melt-interface positions

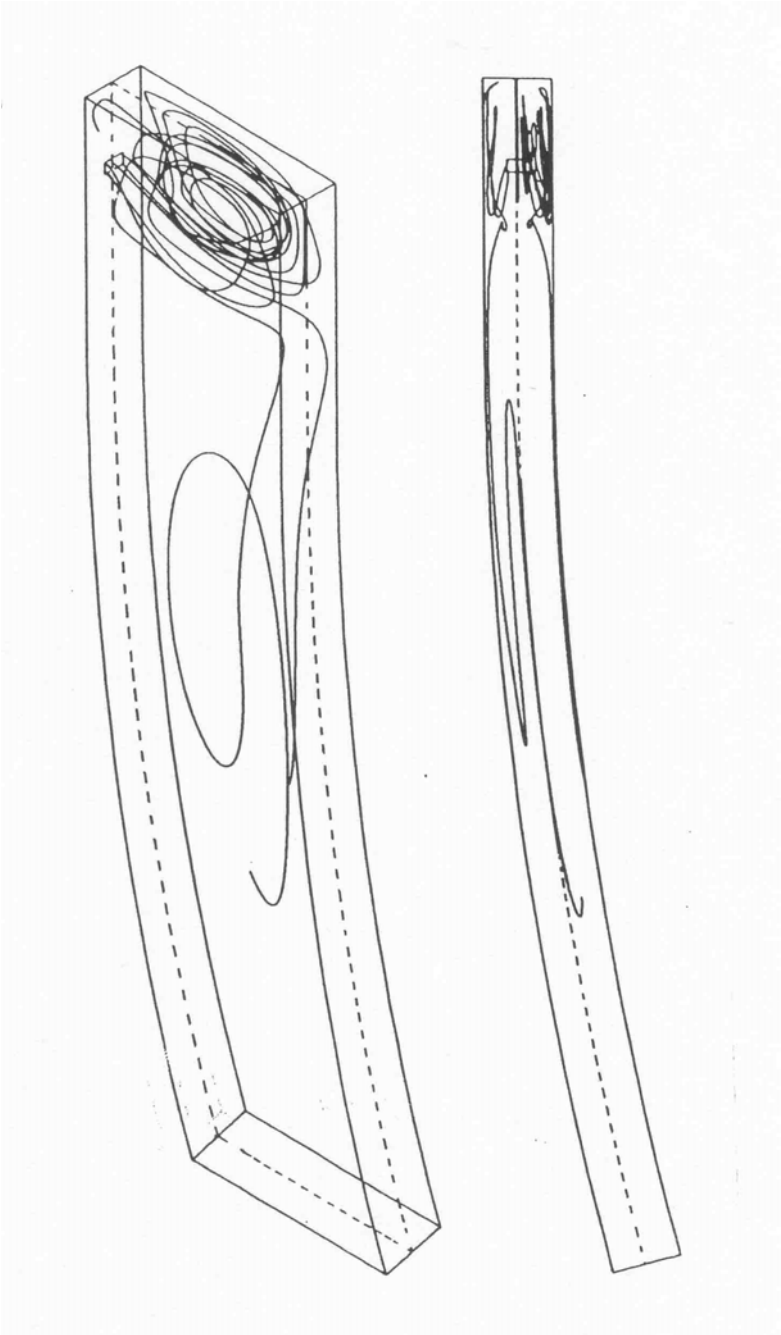

Fig. 9 Sample trajectories of five 208-micron solid alumina inclusion particles

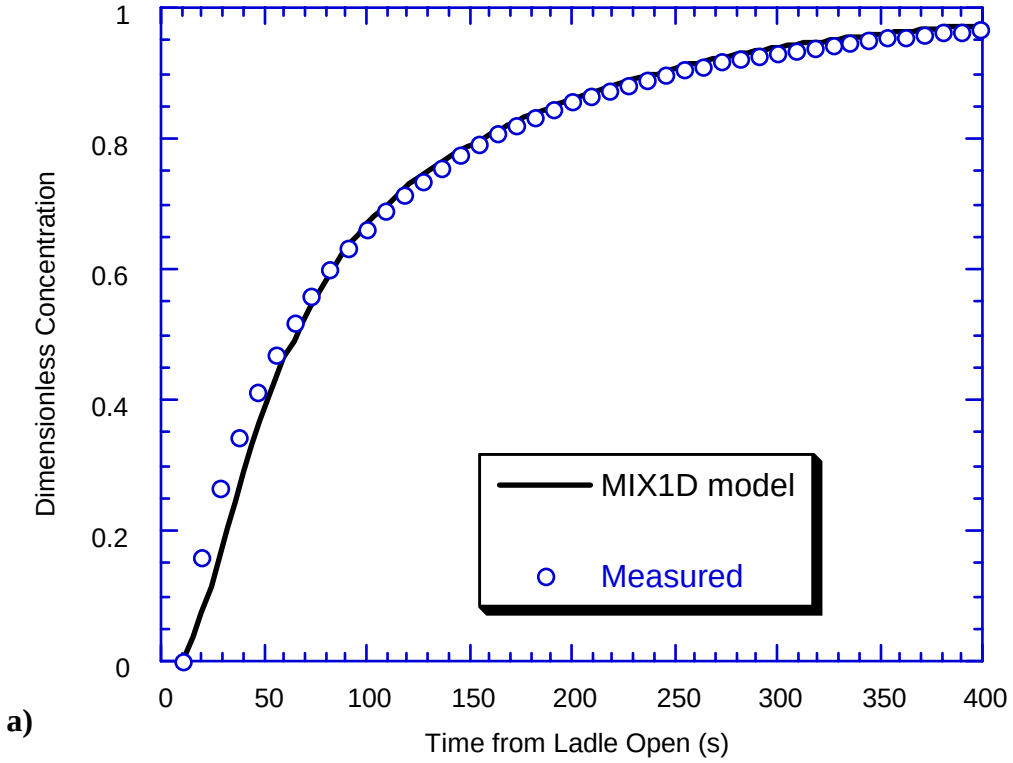

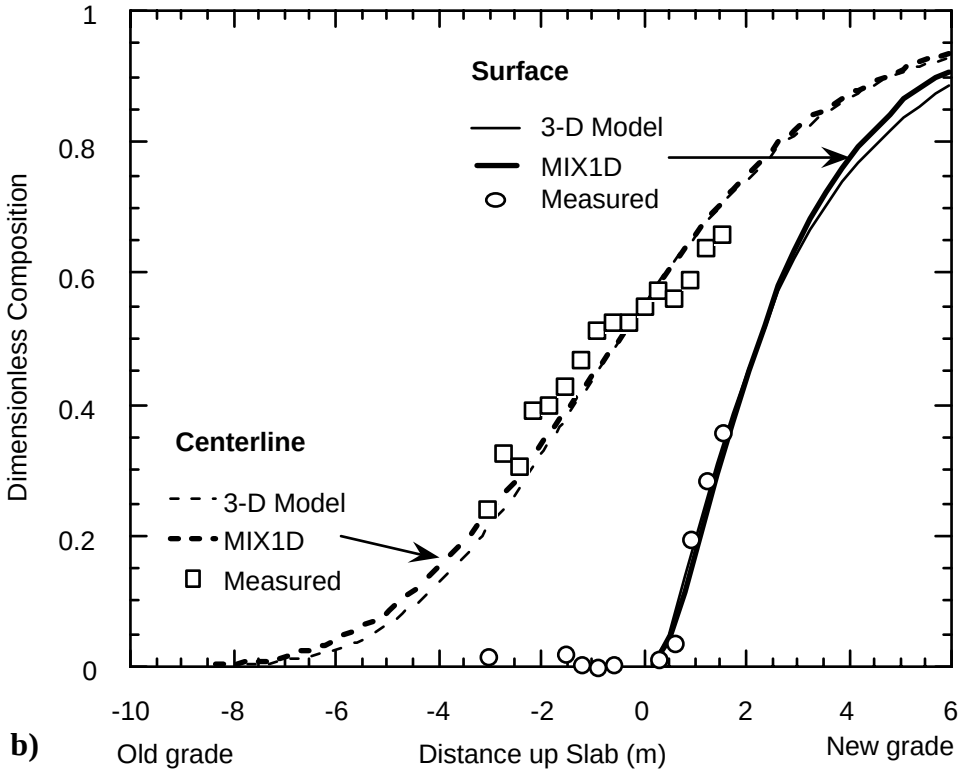

Fig. 10 Predicted intermixing during a grade change compared with experiments

a) Composition history exiting tundish into mold

b) Composition distribution in final solid slab

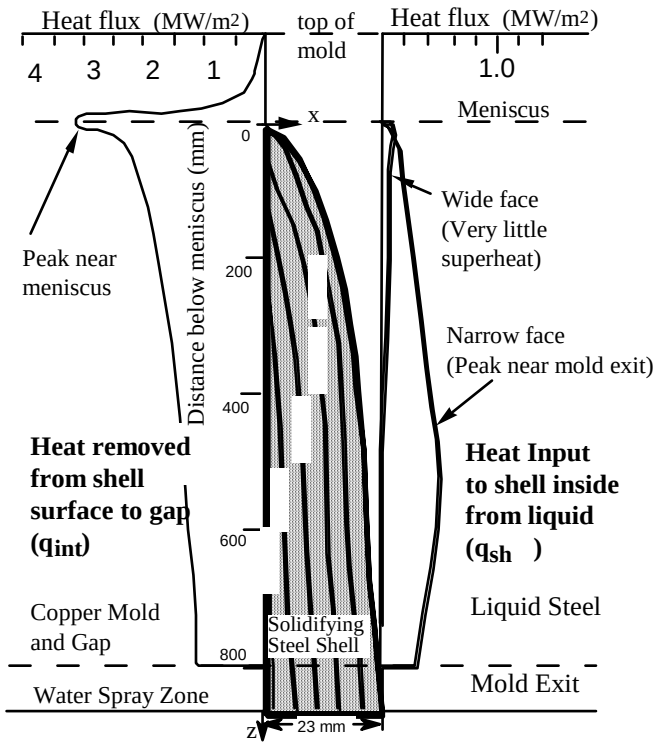

Fig. 11 - Typical isotherms and boundary conditions calculated on shell solidifying in mold

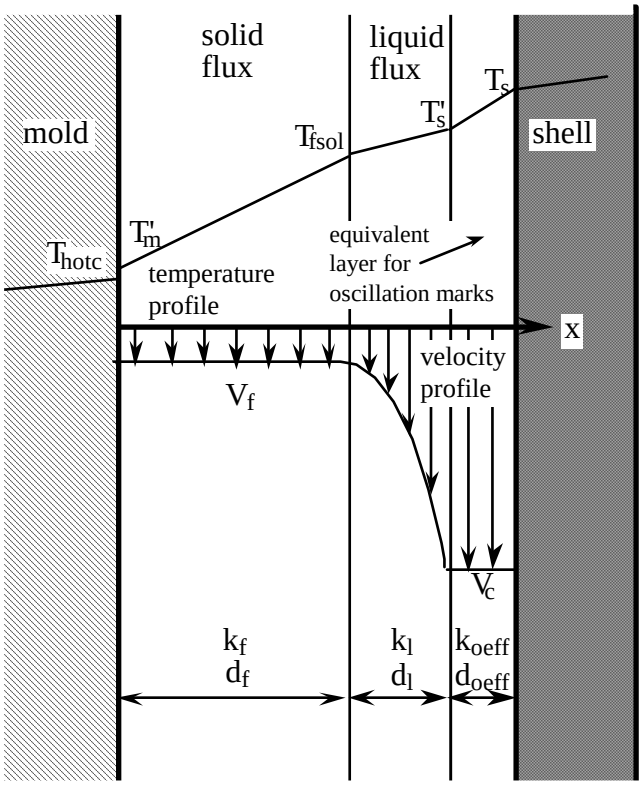

Fig. 12 Velocity and temperature profiles across interfacial gap layers (no air gap)

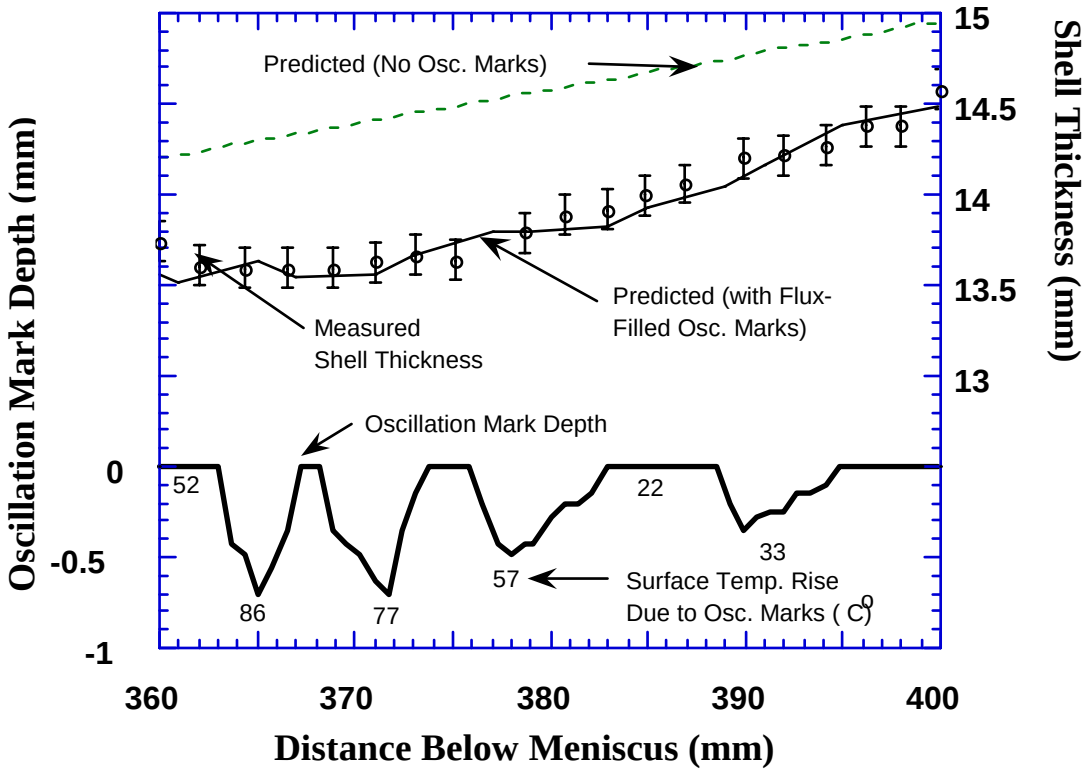

Figure 13 - Comparison of predicted and measured shell thickness with oscillation mark profile and surface temperatures for large, flux-filled oscillation marks

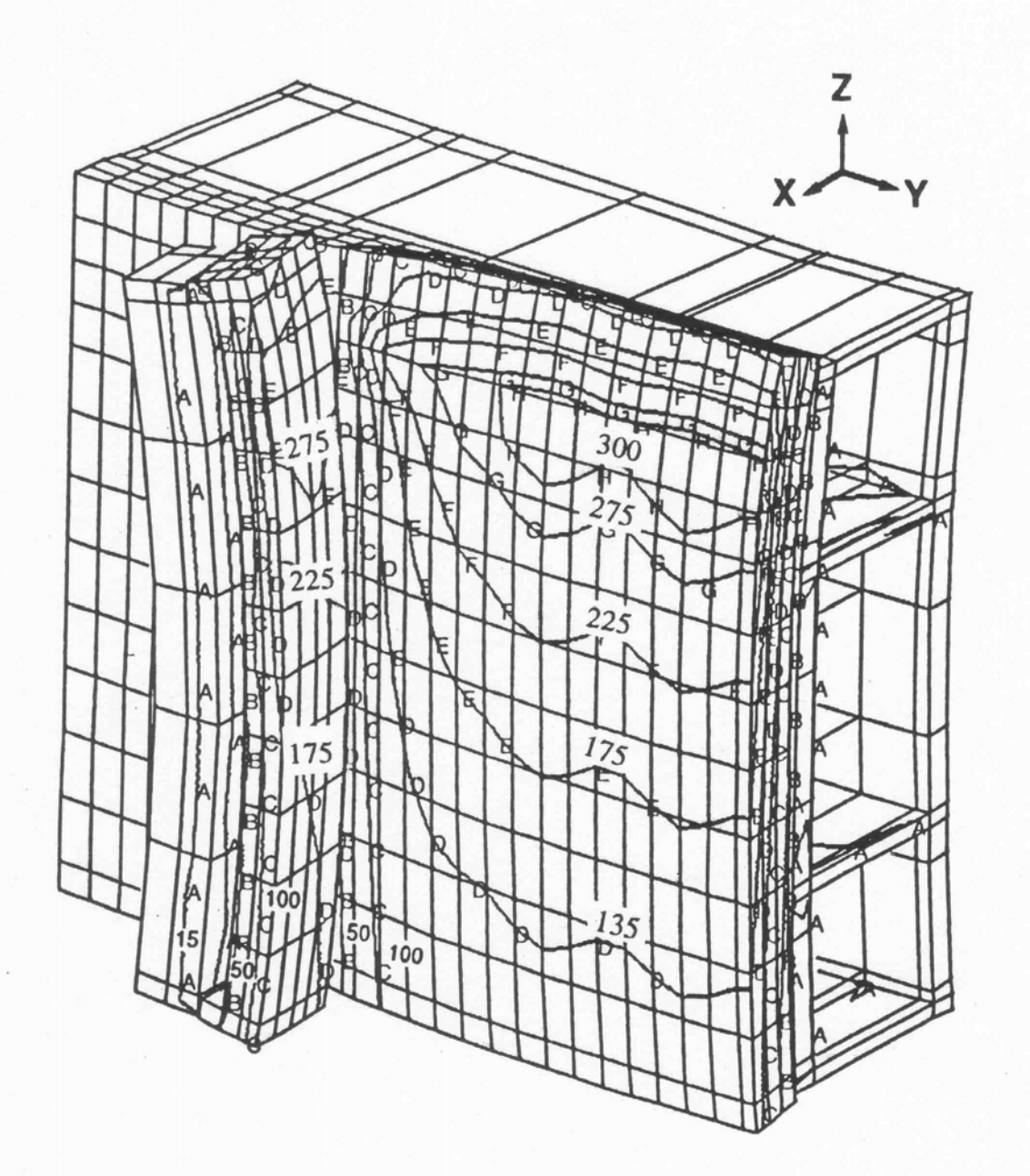

Fig. 14 - Distorted mold shape during operation with temperature contours (˚C)

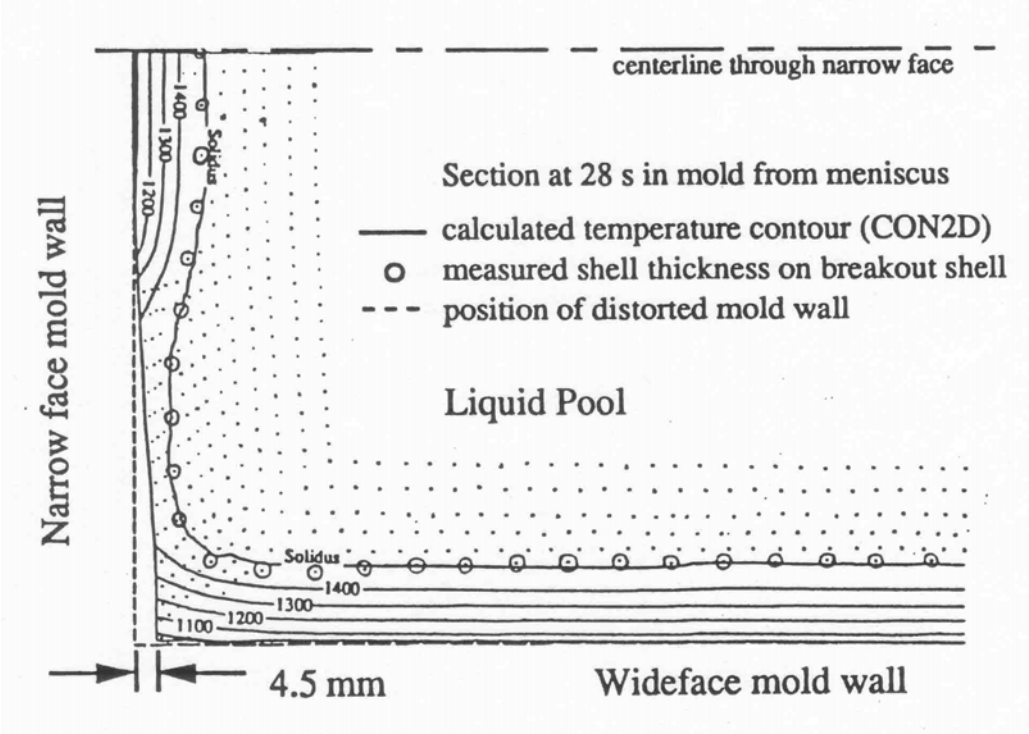

Fig. 15 Comparison between predicted and measured shell thickness in a horizontal (x-y) section through the corner of a continuous-cast steel breakout shell

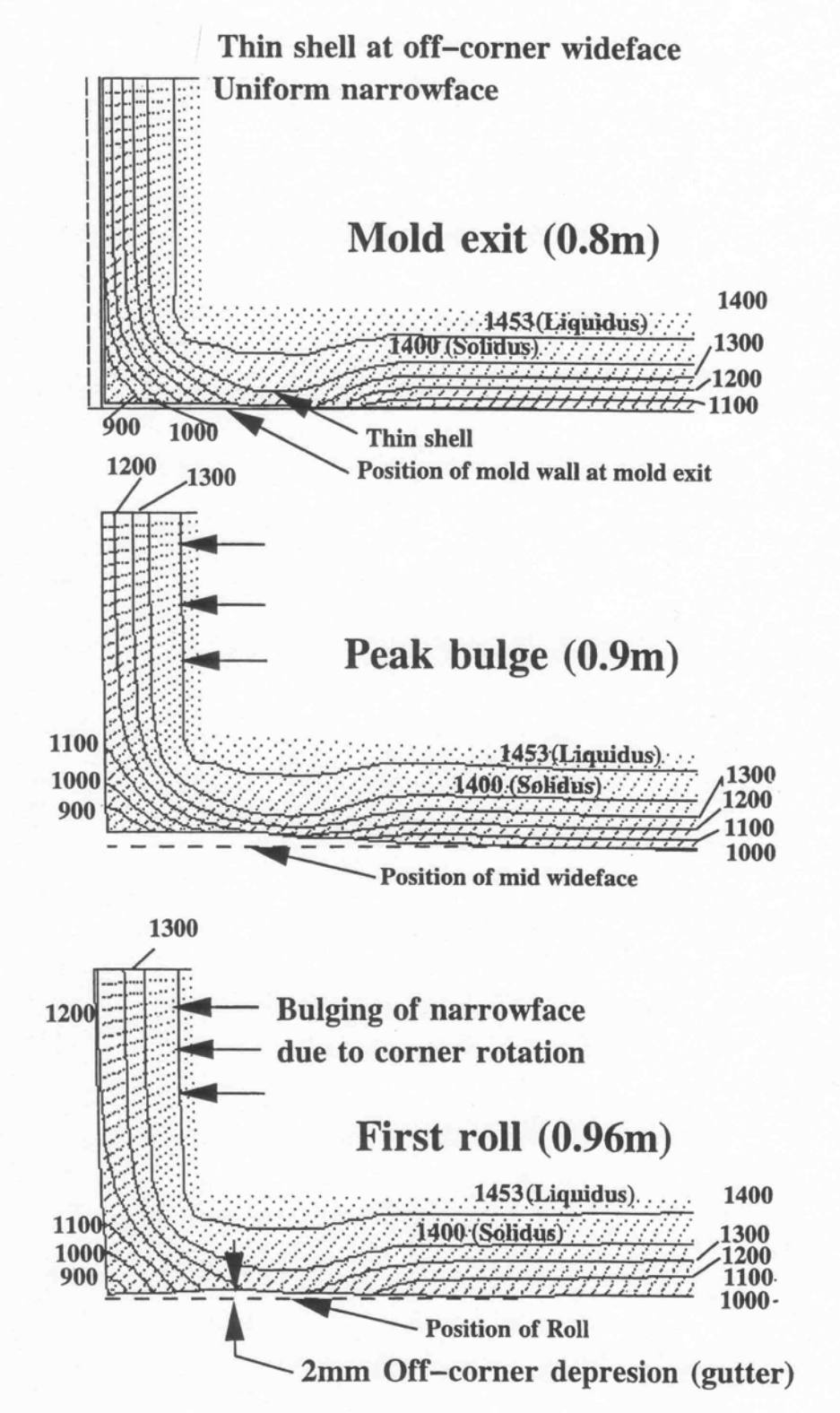

Fig. 16 Calculated evolution of shape of shell below mold (to scale) with isotherms (˚C)

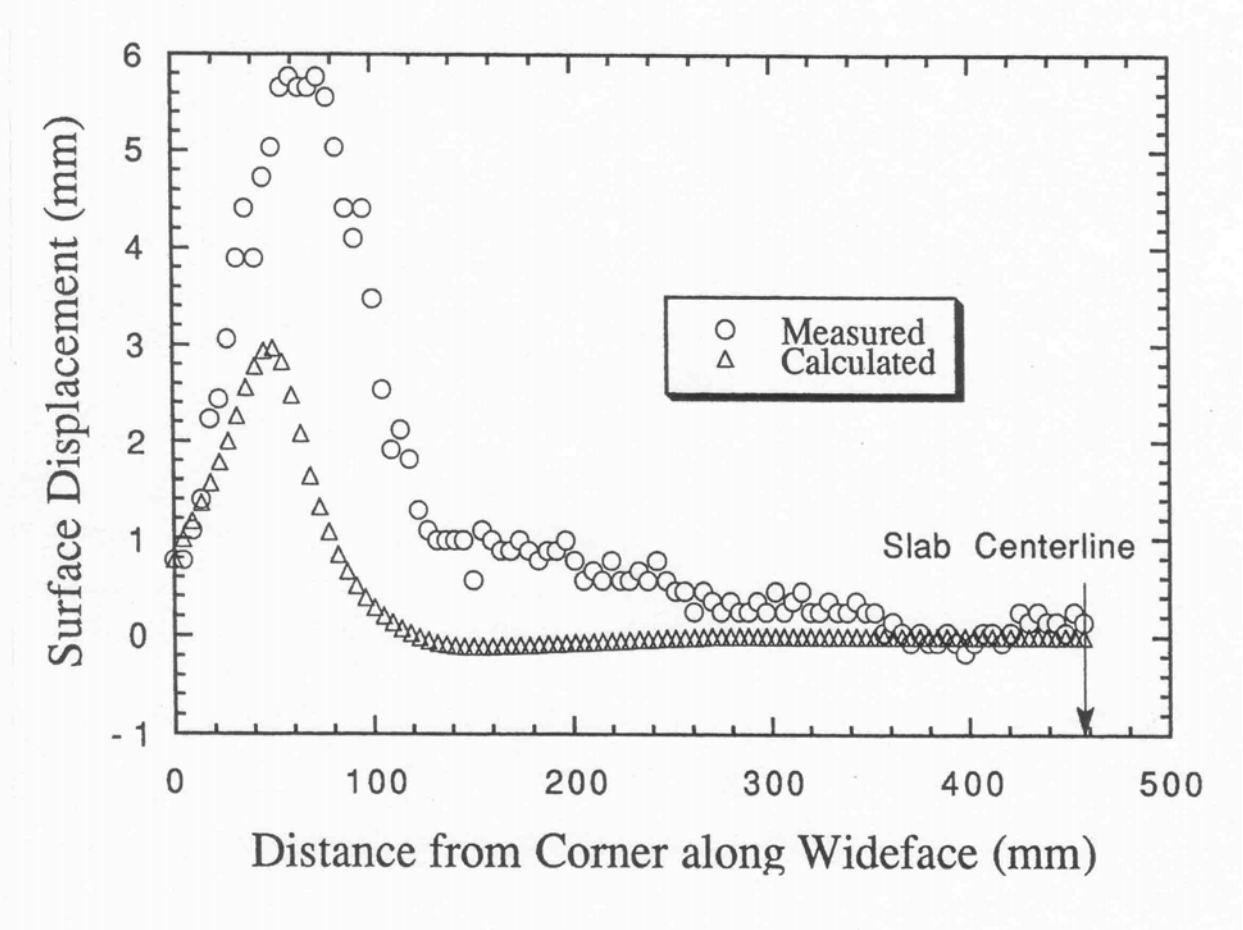

Fig. 17 Comparison of calculated and measured surface shape profile across wideface, showing gutter

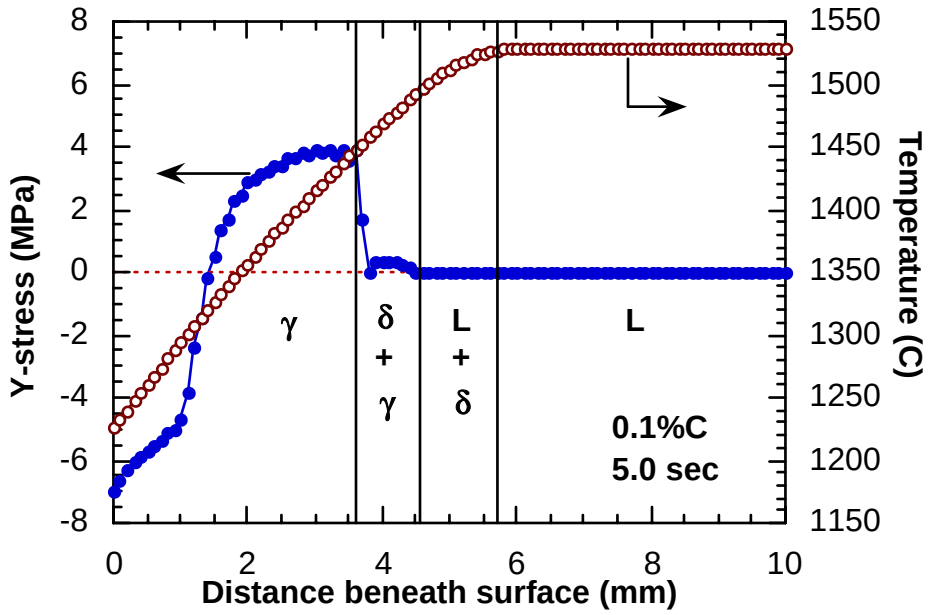

a)

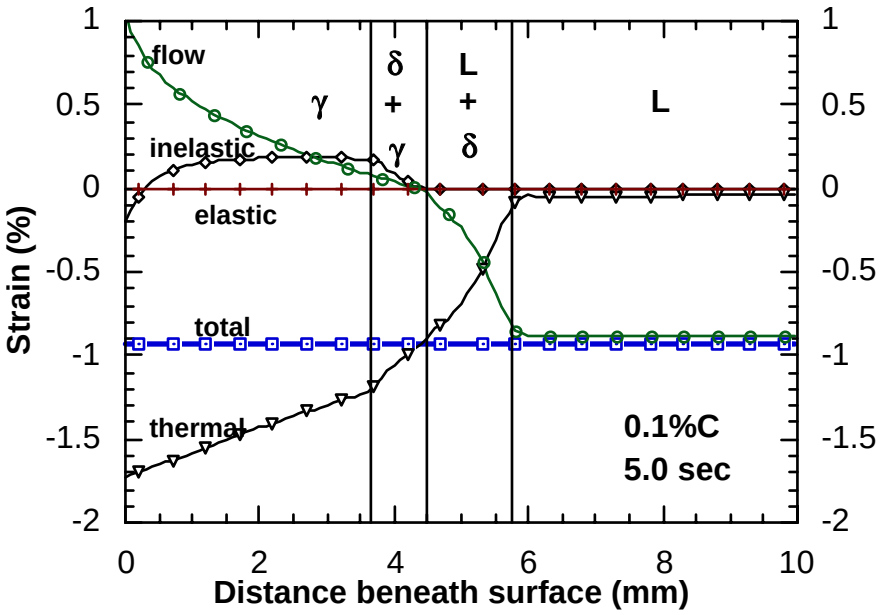

b)

Fig. 18 Typical Temperature, Stress, and Strain distributions through shell thickness [61]

a) stress and temperature profiles

b) strain components